Available online at www.sciencedirect.com

ScienceDirect

Journal of Materiomics 1 (2015) 3–21

www.ceramsoc.com/en/

www.journals.elsevier.com/journal-of-materiomics/

Strain-based scanning probe microscopies for functional materials, biological structures, and electrochemical systems

Jiangyu Li [a,*], Jing-Feng Li [b], Qi Yu [b], Qian Nataly Chen [a], Shuhong Xie [c]

[a] Department of Mechanical Engineering, University of Washington, Seattle, WA 98195-2600, USA

[b] State Key Laboratory of New Ceramics and Fine Processing, School of Materials Science and Engineering, Tsinghua University, 100084 Beijing, China

[c] Key Laboratory of Low Dimensional Materials and Application Technology of Ministry of Education, School of Materials Science and Engineering, Xiangtan University, Xiangtan 411105, Hunan, China

Received 14 December 2014; revised 17 January 2015; accepted 30 January 2015
Available online 27 March 2015

Abstract

Strain and electromechanical coupling are ubiquitous in nature, and exist in many processes involved in information technology, energy conversion, and biological phenomena. Strain-based scanning probe microscopy (s-SPM) techniques, especially piezoresponse force microscopy (PFM) and electrochemical strain microscopy (ESM), have emerged as powerful tools to probe and manipulate materials, structures, and systems at the nanoscale. In this review, we will present the fundamentals of s-SPM and a variety of its operational modes, introduce its applications in scientifically or technologically important functional materials, electrochemical systems, and biological structures, and discuss some of its challenges and potential opportunities. By detecting dynamic strains associated with underlying microscopic processes excited by a scanning probe, high sensitivity and unprecedented spatial resolution can be obtained, though caution must be exercised to distinguish different microscopic mechanisms, and quantitative interpretation of the s-SPM data remains challenging. We expect that s-SPM will continue to provide great insight into functional materials and structures, and will play a valuable role in the emerging field of materiomics.

Keywords: Scanning probe microscopy; Piezoresponse force microscopy; Functional materials; Electrochemical systems; Microstructures

1. Introduction

Driven by the rapid advances in nanostructured materials and systems over the last two decades, scanning probe microscopy (SPM) has emerged as a powerful tool to probe and manipulate materials, structures, and systems at the nanoscale. While SPM was originally developed in the 1980s to study the atomic forces between samples under investigation and a scanning probe tip, a variety of other imaging modes of SPM have since been proposed and implemented, expanding the capabilities of SPM to a wide range of functional properties. Of particular interest here are strain-based SPM (s-SPM) techniques that detect dynamic strain excited in a sample using a scanning probe, including piezoresponse force microscopy (PFM), conceived in 1990s [1,2], and recently developed electrochemical strain microscopy (ESM) [3,4] and piezomagnetic force microscopy (PmFM) [5,6]. These techniques have been applied to study functional materials such as piezoelectrics, ferroelectrics, and multiferroics, electrochemical devices including lithium ion batteries and solid oxide fuel cells, as well as biological materials and structures. They have not only provided unprecedented insights into the microscopic mechanisms of these materials at the nanoscale, but also enabled new discoveries as well as novel nanostructure fabrications and manipulations. Thus we feel it is quite appropriate and timely for us to survey the current state of art of s-SPM in this inaugural issue of Journal of Materiomics.

Strain is ubiquitous in nature, and exists in many processes involved in information technology, energy conversion, and

* Corresponding author.
E-mail address: jjli@uw.edu (J. Li).
Peer review under responsibility of The Chinese Ceramic Society.

http://dx.doi.org/10.1016/j.jmat.2015.03.001

biological phenomena. Many of the strains are electromechanical in nature, and the coupling between electric field and mechanical deformation underpins the functionality of materials and systems as diversified as ferroelectrics and multiferroics, electrochemical cells, and biological systems. In ferroelectrics, strain is directly coupled to polarization [7], and thus can be used to study complex phenomena involving polarization reversal, domain wall pinning, and multiferroic interaction. During electrochemical conversion and transport, a key attribute is electrochemical strain resulting from changes in either ionic concentration or valence state [8–12], which might not be desirable for device operation, yet provide valuable information on local electrochemistry that is otherwise difficult to detect. The very basis of biological functionalities is electromechanics [13–15], including nerve-controlled muscle contraction at macroscale, hearing at microscale, and voltage-controlled ion channels at nanoscale. It appears that strain and electromechanical coupling are directly relevant to many existing and emerging aspects of materials science and nanobiotechnology, and s-SPM techniques, by detecting dynamic strain associated with underlying microscopic processes, offer a set of power tools to probe such materials and systems with high sensitivity and resolution.

In this short review, we will present the fundamentals of s-SPM and a variety of its operational modes, introduce its applications in a number of scientifically or technologically important areas, and discuss some of its challenges and potential opportunities. This does not mean to be a comprehensive survey of the state of art. Instead, we plan to sample some of the progress in methodology development, present selected applications in functional materials, electrochemical systems, and biological structures, and highlight a few endeavors in resolving microscopic mechanisms and quantitative analysis associated with s-SPM.

2. Fundamentals of strain-based scanning probe microscopies

2.1. Basic operations

Scanning probe microscopy (SPM) was developed to detect tiny interactions between a scanning probe tip and the sample surface under investigation. As shown in Fig. 1(a), an SPM system includes four core components: (1) a cantilever that serves as a force sensor; (2) a laser photodiode that measures cantilever deflection; (3) a scanner that moves the sample relative to the cantilever in two-dimensions (2D); and (4) a data acquisition and control unit. When the cantilever is brought close to the sample surface by an actuator in the z direction, the interaction between the probe tip and the sample surface will attract or repel the cantilever, resulting in a deflection s that is measured by photodiode. If the spring constant k of the cantilever is known or calibrated, then the interaction force can be calculated as

$$F = ks. \tag{1}$$

Meanwhile the displacement Z of the entire cantilever along the z axis is independently controlled, and the tip-sample distance D can be determined as

$$D = Z + s \tag{2}$$

when an appropriate sign convention is adopted, allowing us to measure the tip-sample interaction force F as a function of their distance D. Interested readers can refer to monograph by Greg Haugstad for more in-depth discussions on SPM [16].

The imaging mechanism of s-SPM is based on the detection of dynamic strain or displacement of the sample. An AC voltage is applied to the sample through the conductive probe in contact with the sample, which often serves as the top electrode, with the bottom electrode grounded underneath the sample, as shown in Fig. 1(b). Since the probe tip is in contact with the sample surface, the cantilever is bent upward, and the set point, i.e. the force exerted by the cantilever to the sample surface, is usually fixed by feedback control. As such, the topography of the sample surface can be mapped simultaneously with the surface displacement. The applied electric field will trigger a localized surface vibration of the sample due to its electromechanical coupling, which in turn induces vibration of the cantilever that can be measured by the photodiode. Two types of surface displacement can be measured, one is the vertical one arising from normal strain, as shown in Fig. 2(a), and the corresponding mode is referred to as vertical s-SPM; the other is the lateral displacement arising from shear strain, as shown in Fig. 2(b), and the corresponding

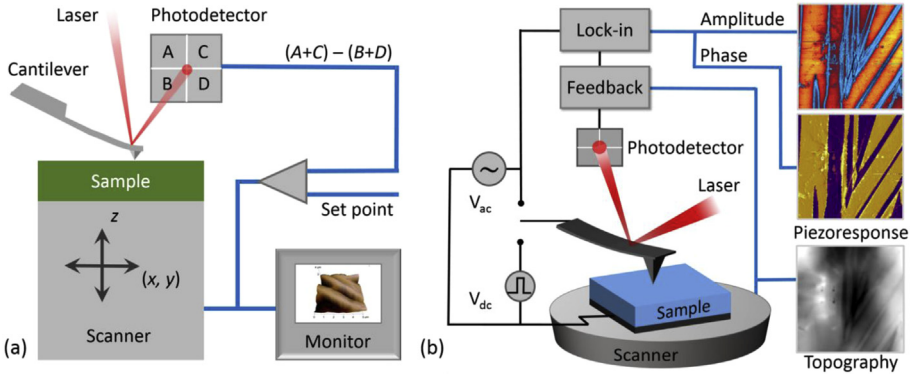

Fig. 1. Configurations of a typical SPM system (a) and s-SPM setup (b).

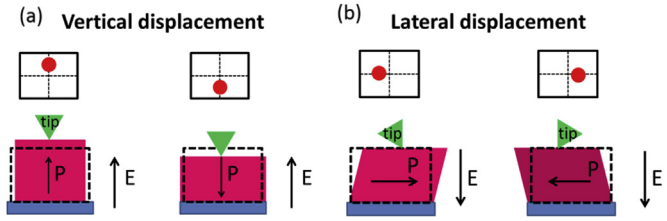

Fig. 2. Schematics of (a) vertical and (b) lateral s-SPM.

mode is referred to as lateral s-SPM. The combination of vertical and lateral s-SPM can provide comprehensive information on the underlying microstructure and microscopic processes, as we discuss later.

In addition to the displacement excited by an electric field, other actuation methods have also been developed. One is based on displacement driven by a piezoelectric transducer underneath the sample [17,18], as shown in Fig. 3(a), and the resulting vibration of the sample surface can be measured, yielding information on the mechanical properties of the sample. Magnetic materials can also be excited by magnetic fields generated by an AC current in a coil, as shown in Fig. 3(b), and this is what we refer to as piezomagnetic force microscopy (PmFM) [5,6]. The imaging mechanism of PmFM is based on the magnetostrictive effect, similar to the detection of piezoelectric strain in PFM. Unlike conventional magnetic force microscopy (MFM), which is based on long-range magnetostatic interactions and requires a magnetized tip and two-pass scans [19], PmFM has advantages in its contact mode operation with a nonmagnetic tip in one-pass.

2.2. Dynamics-based techniques

The surface displacements induced under s-SPM are usually very small, in the range of picometers (pm), and thus it is necessary to amplify the displacement to enhance the sensitivity. This is often accomplished by exciting the surface vibration at the cantilever-sample resonance and measuring the resulting displacement using a lock-in amplifier at the driving frequency, as shown in Fig. 1(b). The details of the digital lock-in are shown in Fig. 4, with which one can obtain not only the amplitude but also the phase of s-SPM response. The lock-in makes it possible to measure the displacement at the frequency of interest with the noise at other frequencies

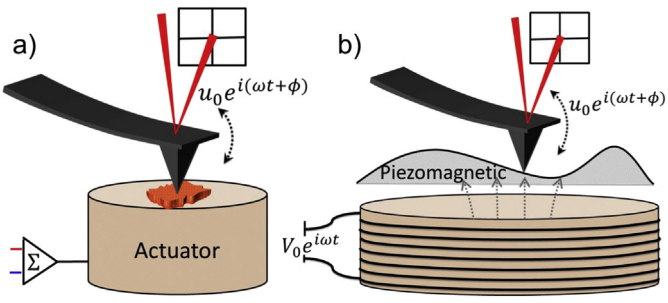

Fig. 3. Schematics of contact resonance method (a) and PmFM (b).

filtered, and thus enhance the signal to noise ratio substantially. The relationship between driving and measuring frequencies can be adjusted, which is important for characterizing nonlinear responses as we show later. When the driving frequency is at the cantilever-sample resonance, the magnitude of the displacement is amplified by orders of magnitude, as shown in Fig. 5(a), making it possible to detect displacements as small as pm. Furthermore, it turns out that the cantilever-sample vibration can be described by the damped driven harmonic oscillator model [20–22], with the s-SPM amplitude A and phase ϕ given by,

$$A = \frac{A_i}{\sqrt{\left(1-\omega^2/\omega_0^2\right)^2 + \left(\omega/\omega_0 Q\right)^2}},$$
$$\phi = \tan^{-1}\left\{\frac{\omega/\omega_0}{Q\left[1-\left(\omega/\omega_0\right)^2\right]}\right\}, \quad (3)$$

where ω and ω_0 are driving and resonant frequencies, respectively, Q is the quality factor, and A_i is the quasi-static amplitude at a frequency far away from the resonance. As seen in Fig. 5(a) and (b), these two equations fit experimental data pretty well. As such, if the s-SPM amplitude and phase can be measured at two or more frequencies, then the resonant frequency, quality factor, as well as phase and amplitude at the resonant frequency can be solved from these two equations, providing us not only the underlying electromechanical coupling of the sample, but also its contact stiffness (through the resonant frequency) and dissipation (through the quality factor). For example, the intrinsic or corrected s-SPM amplitude A_i in the absence of resonance enhancement can be determined by dividing the resonant amplitude A_0 by the quality factor,

$$A_i = \frac{A_0}{Q}, \quad (4)$$

which reflects the intrinsic electromechanical response of the sample.

In order to maintain high sensitivity, it is necessary to drive the AC voltage at cantilever-sample resonant frequency, as we discussed above. However, during scanning, the resonant frequency often shifts due to changes in contact stiffness, which may arise from material heterogeneity or topography variation. So it is necessary to track the resonant frequency during scanning, and there are two main techniques to accomplish this. The first is the dual amplitude resonance tracking (DART) technique, which was previously referred to as the dual frequency resonance tracking (DFRT) technique [23]. In this approach, the cantilever-sample system is driven at two different frequencies across resonance, as shown in Fig. 6(a), and the resulting amplitudes at these two frequencies are maintained to be equal. When the resonant frequency shifts within a certain range, one frequency will become closer to the resonance, and its amplitude will increase. The other frequency moves in the opposite direction and its amplitude will decrease. The difference between these two amplitudes serves

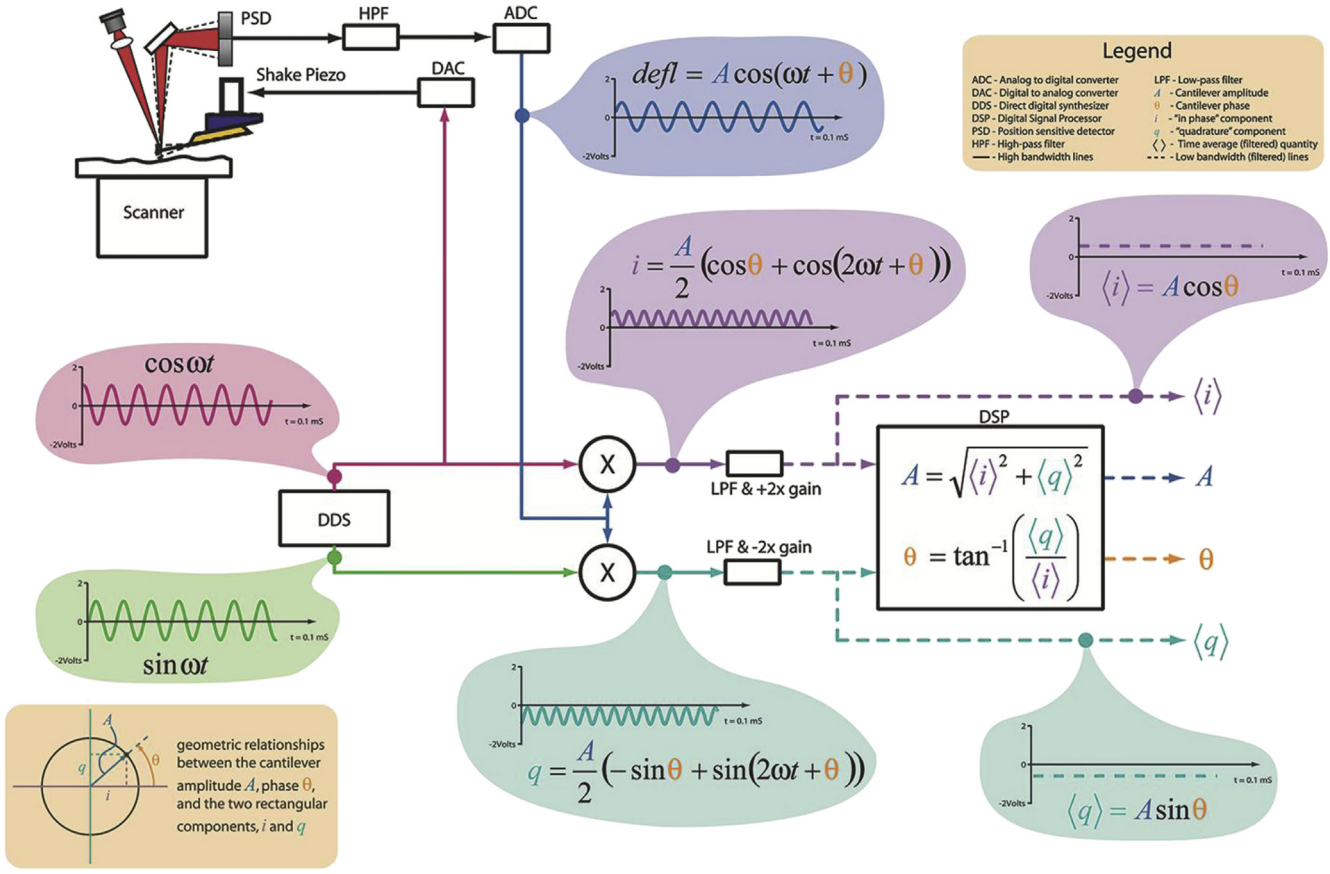

Fig. 4. The schematic of digital Lock-in and flow chart of data processing; courtesy of Asylum Research, an Oxford Instruments company, Santa Barbara, CA.

as feedback control to adjust the driving frequency, so that the resonant frequency can be followed during scanning, as long as the shift is not too large. Loss of resonance tracking does occur in practice when large resonance shifts are encountered. As we discussed above, measuring the amplitudes and phases at two frequencies during scanning enables us to derive mappings of resonant frequency and quality factor by solving Eq. (3), and examples of such mappings are given in Fig. 6.

Another technique is based on band excitation (BE) [24]. Instead of using two driving frequencies, a band of frequencies within a range is applied to drive the cantilever-sample system, as shown in Fig. 7. The driving signal in frequency domain is first inversely Fourier transformed into time domain, and applied to the scanning probe. The resulting response in the time domain is recorded and Fourier transformed back into frequency domain, yielding response at each driving frequency, which can be fitted by Eq. (3) to yield the system parameters of interest, similar to what we have discussed for DART technique. Band excitation (BE) eliminates the need to track the resonance, as long as the band is sufficiently wide. The disadvantage is that the driving power is distributed over a frequency band, and thus reduces the response at each driving frequency. The resulting signal is not filtered through the lock-in either, affecting its signal to noise ratio.

Most of the time, the excitation of the cantilever-sample system and the detection of the corresponding response

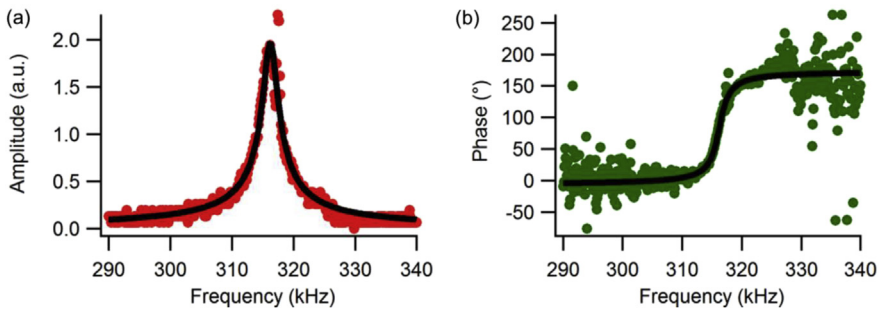

Fig. 5. Amplitude (a) and phase (b) of s-SPM response versus driving frequency.

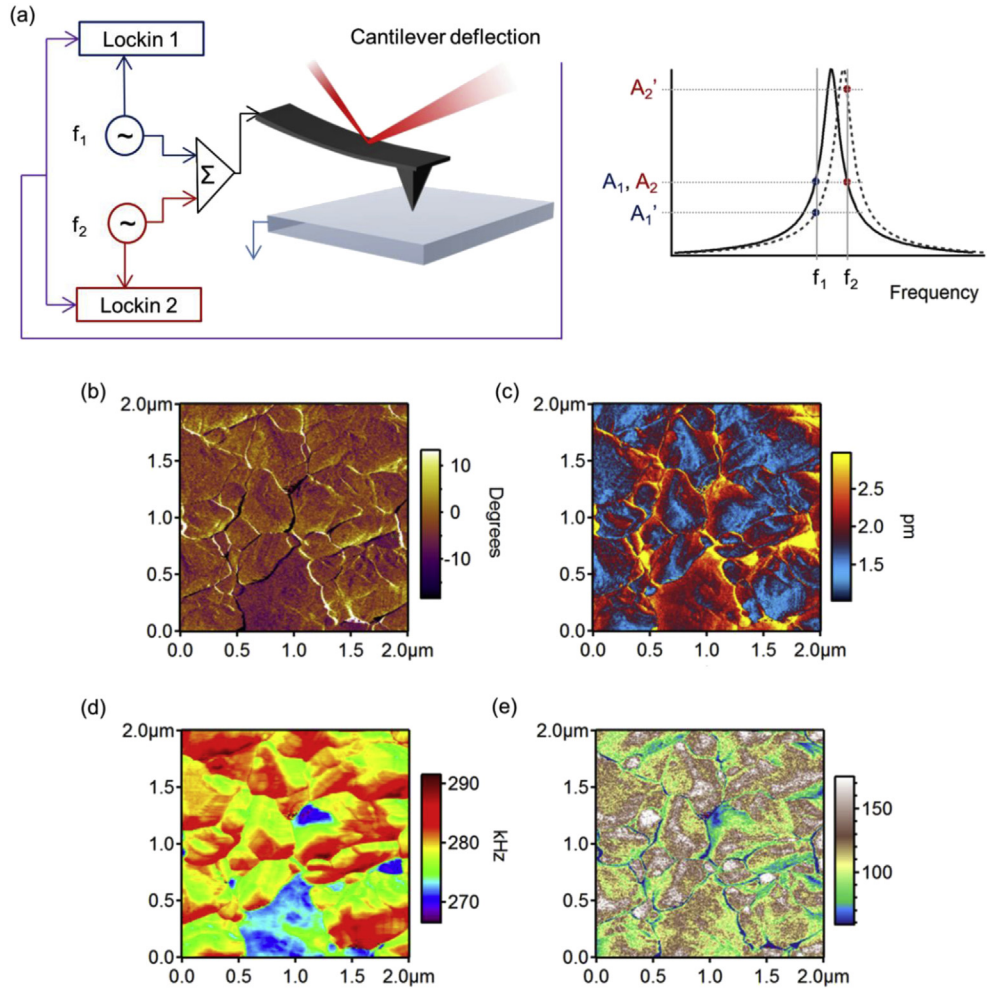

Fig. 6. (a) Schematic of DART technique; and the mapping of phase (b), amplitude (c), resonant frequency (d), and quality factor (e) determined from DART s-SPM.

occur at the same frequency, usually the resonant frequency for enhanced sensitivity, as shown in Fig. 5. This is the so-called first harmonic technique, with which the response linear to the excitation is detected, appropriate for materials such as piezoelectrics wherein the strain is proportional to electric field. On the other hand, nonlinear effects are of interest in many systems, for example in ferroelectrics, and this requires higher harmonic detection. In the second harmonic

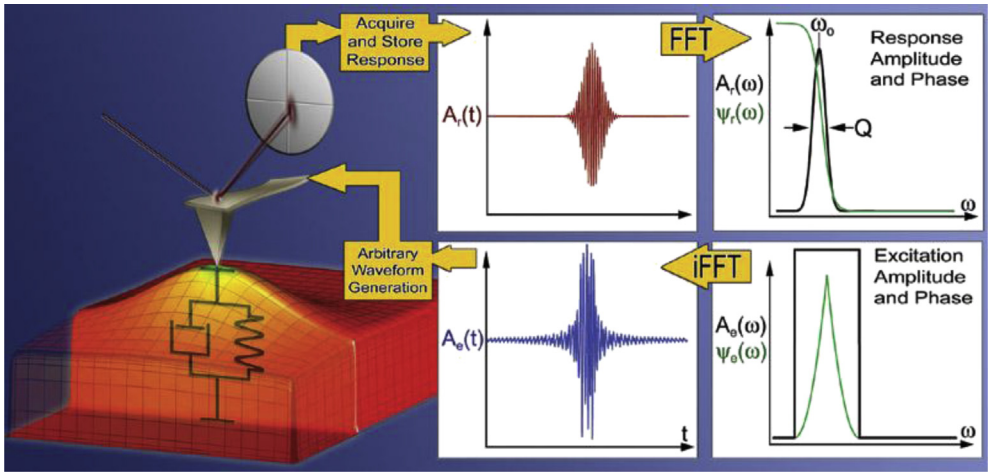

Fig. 7. Schematics of band excitation technique. Reprinted with permission from Ref. [24], Nanotechnology 2007:18:435503.

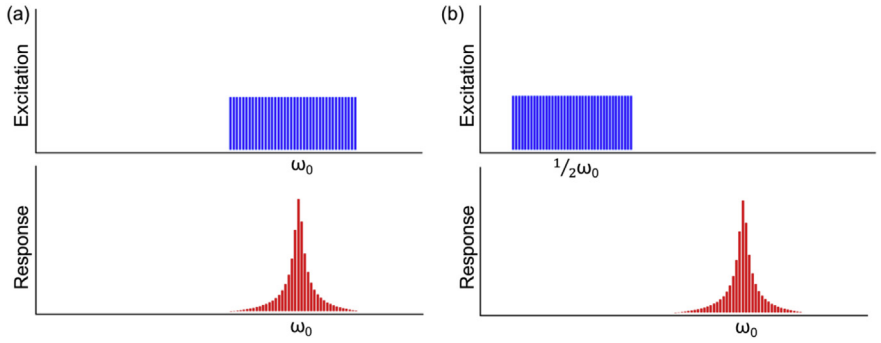

Fig. 8. Schematics of (a) first and (b) second harmonic techniques.

technique, the excitation is driven at $\omega/2$, while the response is detected at ω, as shown in Fig. 8, so that the strain quadratic to the applied electric field is measured [25,26]. To enhance the sensitivity, the system is usually excited at $\omega_0/2$, so that the measurement is carried out at resonant frequency ω_0. Second harmonic detection can be realized in single frequency and BE modes, and higher harmonic techniques can be implemented accordingly if of interest.

2.3. DC-based manipulations

In addition to exciting surface vibration of a sample using AC voltages, DC voltages can also be applied to manipulate the state of the sample. This is often carried out in two different waveforms. In the first type, a sequence of DC voltages in triangular waveform is applied, on top of which AC voltage is simultaneously exerted to excite surface vibration, as shown in Fig. 9(a). For ferroelectric materials, the sequence of DC voltages would switch the polarization of the sample when the coercive field is exceeded, and this is referred to as switching spectroscopy PFM (SSPFM) [27]. Between each DC voltage step, the so-called ON state, the voltage is stepped back to OFF state with zero voltage, and the response is usually measured during the OFF state to minimize the electrostatic interactions between the probe and sample. For the second type, more appropriate for electrochemical systems, DC voltages in square wave forms are applied over longer periods of time, as shown in Fig. 9(b), and this would trigger longer range electrochemical activities, for example surface reactions or ionic diffusions depending on the polarity of the DC voltage. Such techniques can be useful for relaxation study after the DC voltage is stepped back to zero, from which a relaxation time constant can be derived that reflects the ionic diffusivity [28].

The DC voltage can also be applied as a nanolithography tool to fabricate a nanostructured pattern. While scanning a desired region on the sample surface, positive and negative voltages can be applied based on a pre-designed template, which changes the sample state accordingly, resulting in a desired structure in the sample. For ferroelectric materials, this corresponds to positively and negatively polarized regions [29], and one such example using the CU Buffaloes logo as template is shown in Fig. 10, where the patterned polar structure is exhibited by both PFM amplitude and phase mappings. For electrochemical systems, this could correspond to oxidized and reduced regions on the sample surface. Based on the patterned surface states, subsequent nanofabrication can also be carried out, as we show later.

3. Applications of strain-based scanning probe microscopies

In the last section, the fundamentals of s-SPM have been introduced, and various operation modes have been discussed. In this section, we focus on the applications of s-SPM for functional materials, biological structures, and electrochemical systems.

3.1. Piezoresponse force microscopy

Piezoresponse force microscopy (PFM) is one mode of s-SPM that was developed for piezoelectric and ferroelectric

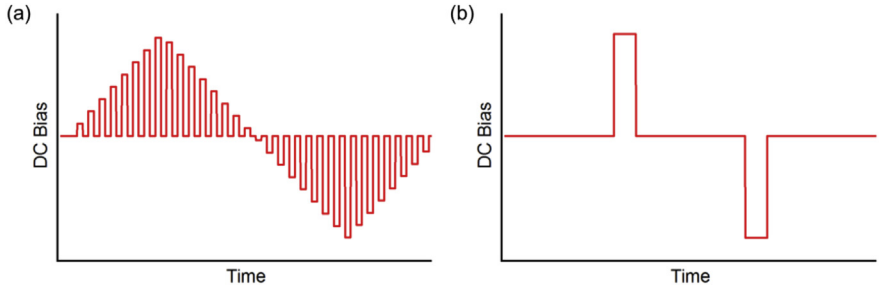

Fig. 9. Voltage profiles for DC manipulations; (a) triangular wave; (b) square wave.

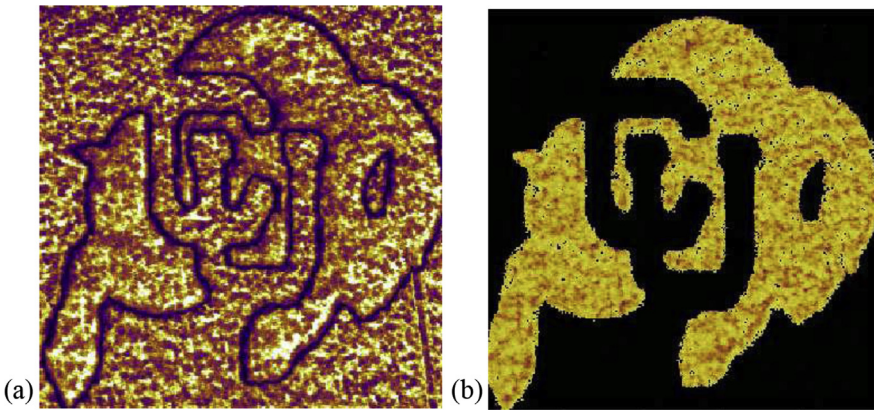

Fig. 10. PFM based nanolithography using a CU buffalo logo as template, with patterned polar structure exhibited by (a) PFM amplitude mapping and (b) PFM phase mapping.

materials. In piezoelectric materials, the strain ε is proportional to the electric field E via the linear piezoelectric coefficient d. For typical piezoelectric ceramics with transversely isotropic symmetry where the polarization is normal to the sample surface, normal strain is induced,

$$\varepsilon_{33} = d_{33}E_3, \tag{5}$$

which can be measured by vertical PFM. On the other hand shear strain is induced

$$\varepsilon_{23} = d_{24}E_2, \quad \text{or} \quad \varepsilon_{13} = d_{15}E_1 \tag{6}$$

when the polarization is in-plane, which can be measured by lateral PFM. To fully characterize in-plane polarization, two measurements have to be carried out, with samples rotating in-plane by 90°. For more general polarization orientation in 3D, vector PFM combining vertical and lateral PFM can be carried out [30]. Interested readers can find more in-depth discussions on PFM in some recent review articles [31–34].

3.1.1. Piezoelectric, ferroelectric, and multiferroic materials

Piezoresponse force microscopy (PFM) has been instrumental in studying piezoelectric and ferroelectric materials, including not only low-dimensional materials and structures made of conventional ferroelectrics, but also new piezoelectric materials and systems, for example two-dimensional materials such as graphene nitride nanosheets [35]. A few recent case studies are highlighted here. One is the molecular ferroelectrics that have attracted significant interest recently, with some of the new molecular crystals exhibiting piezoelectric and ferroelectric properties comparable to their inorganic counterparts [36–38]. For example, it was discovered that diisopropylammonium bromide (DIPAB), a molecular crystal processed from aqueous solution, is ferroelectric with a spontaneous polarization of 23 μC/cm^2, and exhibits good piezoelectric response and well-defined ferroelectric domains [39,40], as shown in Fig. 11. It was observed that phase and amplitude mappings obtained with vertical and lateral PFM overlaid on 3D topography correspond to each other well, revealing ferroelectric domain patterns with alternating bands of upward and downward polarizations separated by domain walls. Upon application of DC voltage under SSPFM, typical PFM hysteresis and butterfly loops are observed, characteristic of ferroelectric switching. Despite the out-of-plane polarization direction of the sample, strong lateral PFM signals exist. This can be understood as arising from nonzero piezoelectric coefficients d_{22} and d_{25} and spontaneous polarization P_2 of C_2 point group, which induce both normal and shear piezoelectric strains simultaneously under an electric field applied along the polar axis. For typical perovskites with out-of-plane polarization, only normal response is expected from symmetry.

Piezoresponse force microscopy (PFM) has also been useful in revealing microscopy mechanisms underlying piezoelectric and ferroelectric properties of samples. One such example involves a series of PZT thin films of different compositions [41], where PFM was used to correlate the subtle relations among composition, microstructure, and ferroelectric properties, as shown in Fig. 12. The evolution of domain structures with composition is evident, resulting in significant differences in PFM butterfly loops at different compositions. A second example is the giant electromechanical response in a mixed-phase rhombohedral-tetragonal $BiFeO_3$ thin film, which was probed using sub-coercive PFM based on multiple-harmonic measurements [42]. Strain and dissipation data, backed by thermodynamic calculations, suggest that the enhanced electromechanical response originates from the motion of phase boundaries. Recently, giant enhancement in ferroelectric retention in $BiFeO_3$ mixed-phase boundaries have also been reported based on PFM experiments [43]. A third example is (K,Na)NbO_3 nanoscale single crystals [44], for which PFM hysteresis and butterfly loops have helped confirm the existence of a morphotropic phase boundary. More examples on PFM applications in piezoelectric and ferroelectric materials can be found in Refs. [45–48].

Multiferroic materials, with coexistence of ferroelectric and magnetic orderings, have attracted significant interest in the past decade [49–51]. Bismuth ferrite is probably the most studied multiferroic material due to its room temperature multiferrocity [52,53], and PFM has been instrumental in

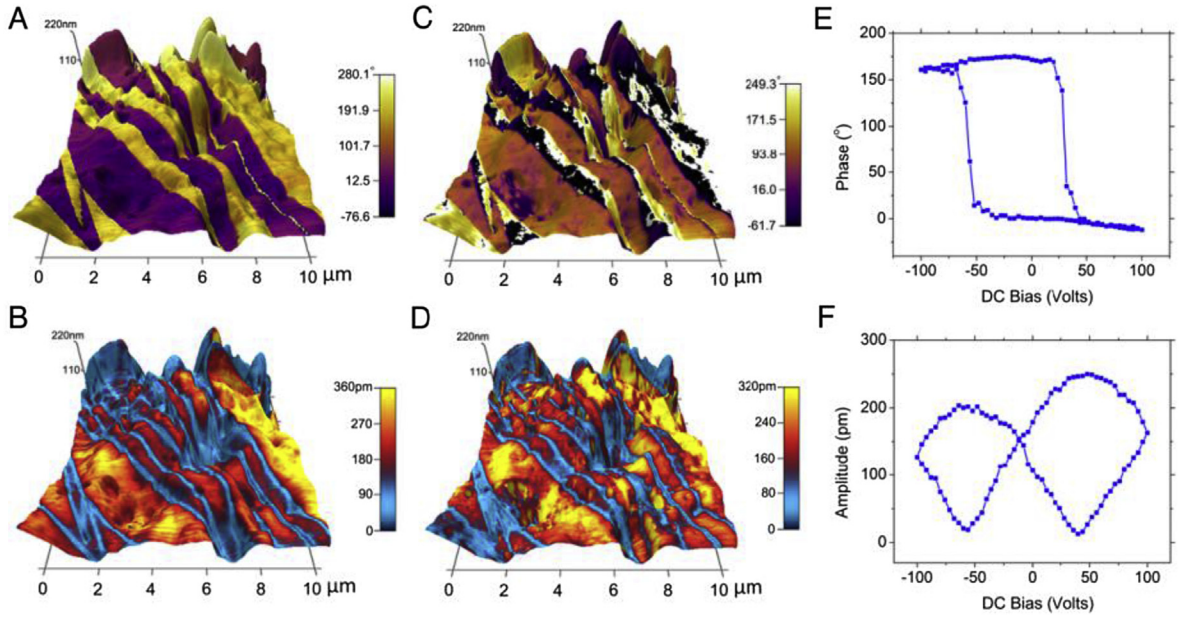

Fig. 11. Piezoresponse force microscopy of DIPAB; (A) amplitude and (B) phase mapping of vertical PFM overlaid on 3D topography; (C) amplitude and (D) phase mappings of lateral PFM overlaid on 3D topography; and (E) phase-voltage hysteresis and (F) amplitude-voltage butterfly loops. From Ref. [39], Science 2013;339:425-8. Reprinted with permission from AAAS.

studying not only its piezoelectric and ferroelectric properties, but also its magnetoelectric coupling. Many interesting phenomena have been demonstrated in $BiFeO_3$ with the help of PFM, including switchable ferroelectric diode and photovoltaic effect [54], a strain driven phase boundary resulting in large piezoelectric strain [55], electric control of magnetic orders [56,57], domain wall conduction [58], and electric modulation of conduction [59]. The domain wall conduction of BFO is shown in Fig. 13, where lateral PFM phase mapping in (a) reveals three types of domain walls, while cAFM mapping in (b) shows conduction at 109° and 180° domain walls, but not 71° domain walls.

For multiferroic composites with strong ferromagnetic phase, PFM has been used to demonstrate magnetic control of ferroelectric domains. This was usually realized by performing PFM and SSPFM under different magnetic fields, as first demonstrated by Xie et al. [60–65]. The setup is schematically shown in Fig. 14 to probe a multiferroic core–shell composite nanofiber, where the magnetic field strength can be adjusted, and notable tuning of PFM butterfly loops is observed, with both coercive field and piezoelectric strain shifted by the magnetic field. The technique has since been applied to demonstrate magnetic field induced polarization reversal in a multiferroic composites [66]. A recent development has involved using both PFM and PmFM to study multiferroic $BiFeO_3$–$LiMn_2O_4$ heterostructure [6], though many challenges remain for PmFM due to the difficulty in localizing a magnetic field with high spatial resolution. If a micro-coil can be implemented on the cantilever to generate a concentrated magnetic field, as recently demonstrated in Ref. [67], PmFM can be valuable for probing multiferroic materials and structures.

Finally, we discuss some examples of PFM nanolithography. This can be carried out by applying a DC voltage

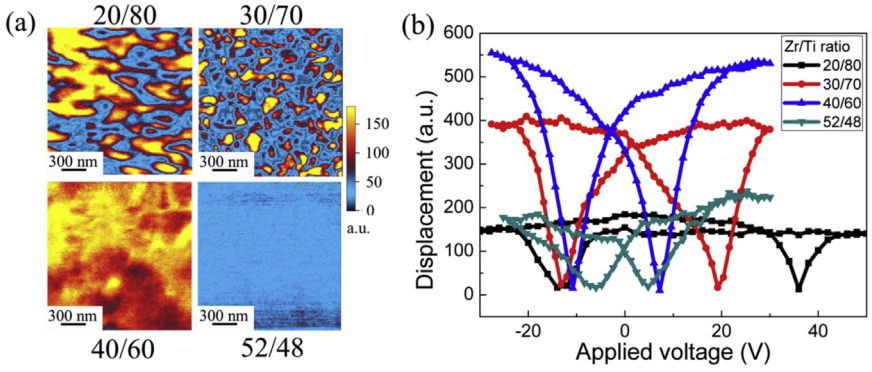

Fig. 12. Domain structure and ferroelectric response of PZT thin film with different Zr/Ti compositions; (a) PFM mappings; (b) PFM butterfly loop. Reproduced from Ref. [41] with permission from The Royal Society of Chemistry.

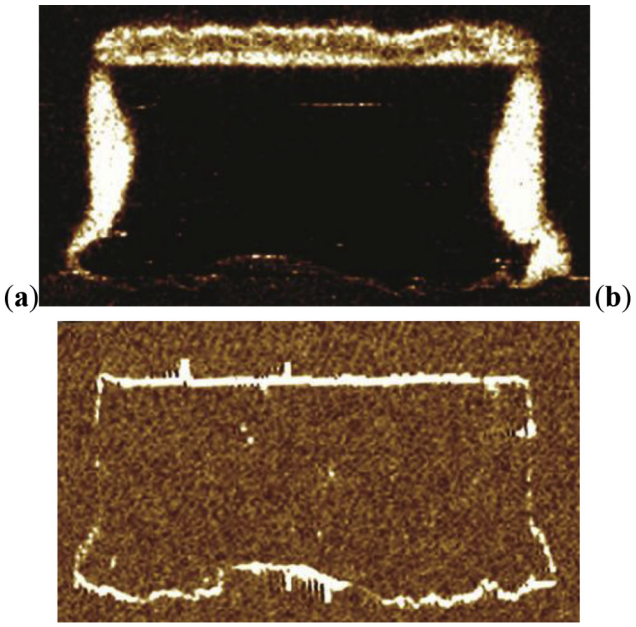

Fig. 13. Domain wall conduction in BFO film; (a) lateral PFM mapping show three types of domain walls; (b) conductive AFM mapping show conduction at 109° and 180° domain walls. Reprinted by permission from Ref. [58], Macmillan Publishers Ltd: Nature Materials 2009;8:229–34, copyright (2009).

at a single point, for example on $BiFeO_3$ thin film to investigate its domain switching dynamics [68a,68b] or to control and manipulate the domain patterns underneath the probe [69] where both vertical and lateral components of electric field can be utilized. More broadly, patterning with positively and negatively polarized structures can be accomplished by scanning with a charged probe [70,71]. One such example is given in Fig. 10. Interestingly, such patterned polar structures can itself be used as template for subsequent deposition of metallic particles [72a–72c]. This is demonstrated in $LiNbO_3$ crystal in Fig. 15. After a domain pattern was written by applying positive and negative voltages while scanning according to the template, visible light-induced polarization-dependent photochemical deposition of silver nanoparticles was realized using the written domain as the template, with the specific deposition of silver nanoparticles on +c domains observed due to the photogalvanic effect of $LiNbO_3$ crystals [73,74]. Such metallic nanoparticle patterns can then be used for surface-enhanced Raman scattering [75–77]. We also point out that it has recently been demonstrated that writing a domain structure by mechanical stress instead of voltage applied through a scanning probe is also possible [78], further expanding the capability of PFM nanolithography.

3.1.2. Biological materials

Many biological tissues are known to be piezoelectric [79–84], including bone, teeth, muscles, nerves, exoskeletons, and otoliths, and piezoelectricity was thought to be a fundamental property of biological systems [85]. It was thus not surprising that PFM has been applied to study a variety of biological materials [86–93], including human bones and teeth, tooth dentin and enamel, collagen fibrils, insulin and lysozyme amyloid fibrils, breast adenocarcinoma cells, and bacteriorhodopsin. While these studies unambiguously confirmed biological piezoelectricity, a closely related phenomenon, ferroelectricity, remains elusive in biology, as no switching behaviors were observed in a number of systems probed, including single collagen. Nevertheless, lateral PFM carried out by Denning et al. [94–96] revealed polarity distribution in rat tail tendon from both amplitude and phase mappings, as shown in Fig. 16, exhibiting polarity contrast in different regions which resembles domain patterns in typical ferroelectrics. Thus it is possible that non-switching in collagen is due to the practical constraint on electric field applicable to the sample instead of fundamental limitations. Interested readers can refer to a recent review article [97] for more discussion on piezoelectric and ferroelectric effects in biology.

The first indication of ferroelectricity in biological tissues was reported by Li and Zeng in green abalone shell, and then in clamshell and nacre shell, as they found consistent PFM switching in these systems [98–101]. Such observation was also reported by Zhou et al. in nacre using a similar technique [102], and ferroelectricity was observed in gamma-glycine as well, the smallest amino acid commonly found in protein [103]. Liu et al. carried out a series of studies on aortic wall and arterial elastin [104,105], and found switching in elastin but not collagen. The ferroelectric switching of elastin has since been confirmed by macroscopic pyroelectric measurement, and its molecular mechanism has been revealed by molecular dynamics simulation [106]. It is interesting to note

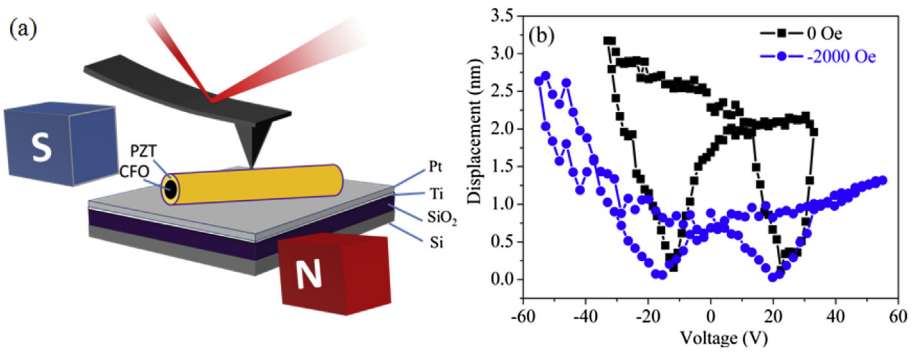

Fig. 14. Probing magnetoelectric coupling by PFM under a magnetic field; (a) schematic setup; (b) tuning butterfly loop by magnetic field.

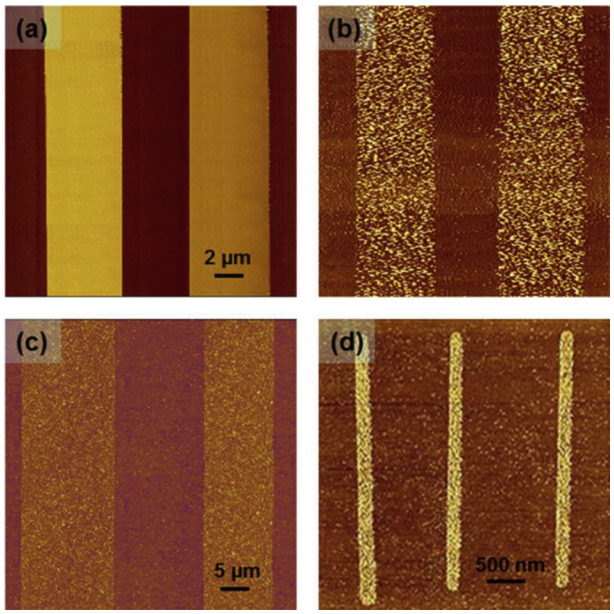

Fig. 15. Demonstrations of selected deposition of Ag nanoparticles on +c domains; (a) PFM mapping of domain structure; (b) deposition of Ag on +c domains; (c) and (d) further examples of selected deposition. For (d), the domains was written by PFM lithography. Reprinted with permission from Ref. [73], Appl. Phys. Lett. 2011;99:053102, Copyright (2011), AIP Publishing LLC.

that ferroelectric switching in elastin is largely suppressed by glucose, as shown in Fig. 17, which could be related to aging, during which glycation between elastin and sugar naturally occurs. Furthermore, we note that nacre shells are switchable, while bones are not. They have similar inorganic constituents, yet different organic components. Bone contains mostly collagens, while shell contains elastic biopolymers such as chitins, which is closer to elastin in its elasticity. Finally, we point out that collagen is a much more ancient protein than elastin, which is only found in arteries of vertebrate and in later stages of embryonic development when blood pressure becomes much higher. Evolution through natural selection may play a role here.

3.2. Electrochemical strain microscopy

Electrochemical strain microscopy was first proposed in 2010 by Balke and Kalinin at Oak Ridge National Laboratory [3,4], and the imaging mechanism, as the name suggests, is based on detection of electrochemical strain. The implementation is very similar to PFM - under an AC voltage, the ionic concentration underneath the scanning probe will fluctuate, resulting in a Vegard strain that is proportional to the ionic concentration change Δn,

$$\varepsilon = \beta \Delta n, \tag{7}$$

where β is Vegard coefficient. This Vegard strain in turn induces a surface vibration similar to piezoelectric strain under PFM, which is detected by the photodiode. While originally proposed to characterize electrochemical activities associated with lithium ions in electrodes and electrolytes of lithium ion batteries, ESM has since been extended to probe other electrochemical systems such as solid oxide fuel cells, which

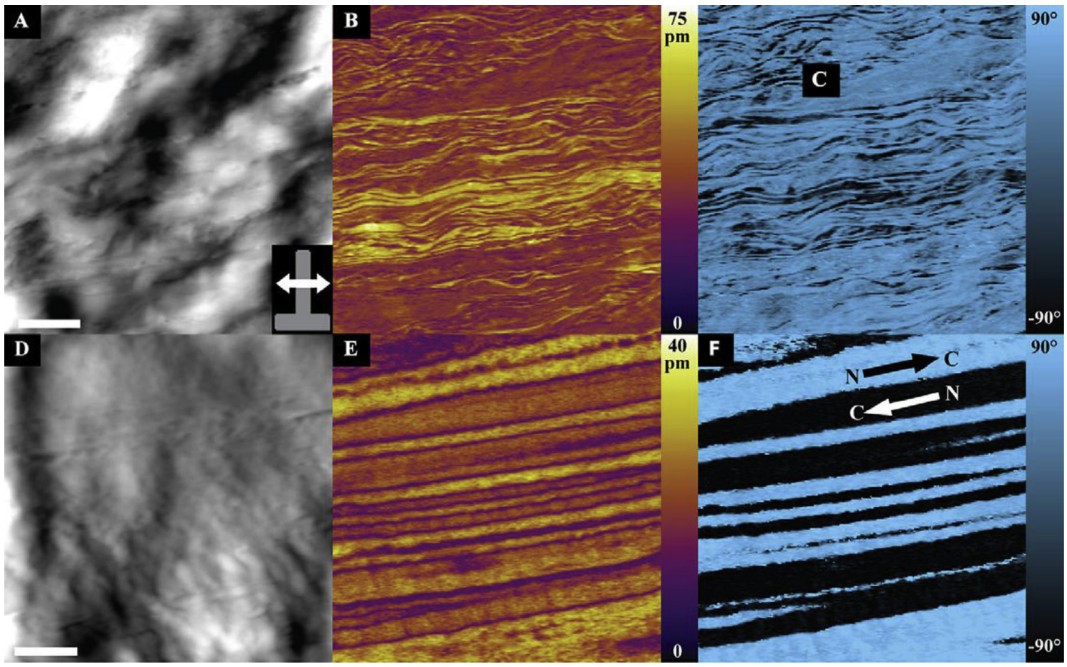

Fig. 16. PFM mappings of rat tail tendon surface. (A) AFM topography, with inset showing cantilever orientation, and scan direction is parallel to the tissue long axis; (B) lateral PFM amplitude of same area as (A); (C) lateral PFM phase image displaying polar orientation of fibrils underneath the surface; (D) AFM topography of a smaller area of tendon obtained from a different location; and (E) lateral PFM amplitude and (F) phase of this area. Scale bar for (A)–(C) is 2 μm, and (E)–(G) is 200 nm. Reprinted from Ref. [94], Journal of Structural Biology 2012;180:409–19, Copyright (2012), with permission from Elsevier.

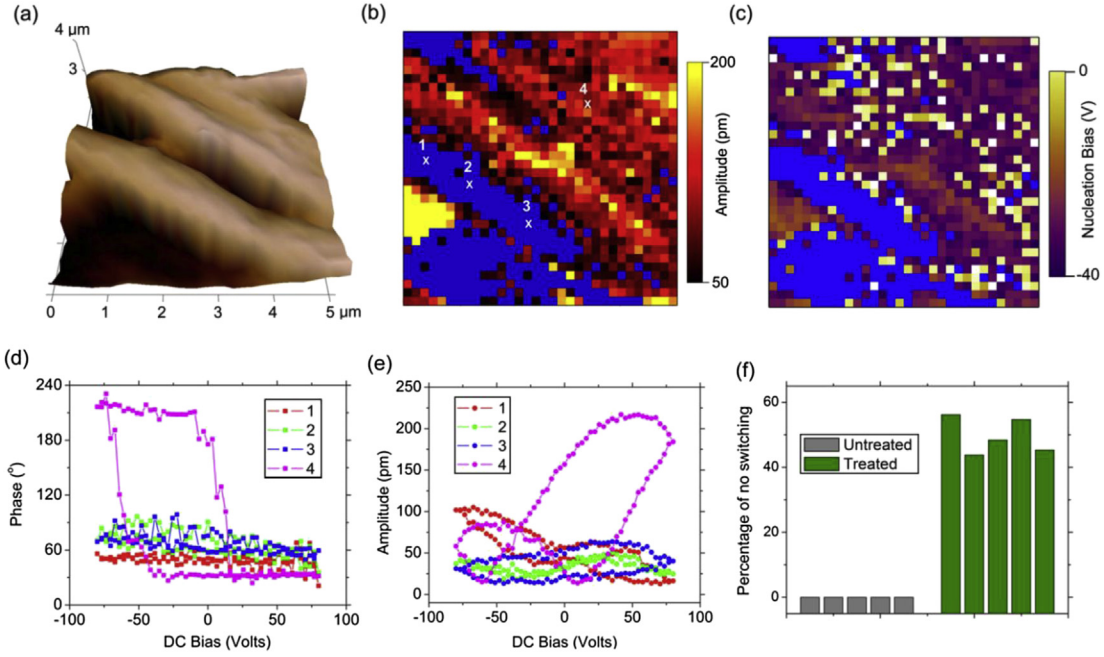

Fig. 17. Switching spectroscopy PFM (SSPFM) mapping of 32 × 32 grid of points over a 5 × 5 μm^2 sample area shows suppression of ferroelectricity in elastin by glucose treatment; (a) 3D topography mapping; and SSPFM mappings of (b) remnant amplitude and (c) nucleation bias, where points with no switching characteristics are marked by blue; (d) phase-voltage loops and (e) amplitude-voltage loops at four representative points, showing that switching is suppressed in points 1, 2, and 3 within the blue area, but is observed in point 4 outside of it; (f) comparison of percentages of points showing no switching characteristics in control and glucose-treated elastin (n = 5) over a 90 × 90 μm^2 sample area, with 64 points probed in each sample; the percentage of the no switching points (49.68% ± 5.54%) in the glucose-treated elastin is significantly higher than the untreated elastin (0%) ($p < 0.05$). Reprinted with permission from Ref. [105], Phys. Rev. Lett. 2013;110:168101. Copyright (2013) by the American Physical Society.

involve for example not only ionic concentration changes but also valence changes and space charges.

3.2.1. Lithium ion batteries

The first model system studied by ESM was amorphous Si anode in an all-solid thin film lithium ion battery, as reported by Balke et al. [3]. By measuring relaxation curves, they demonstrated high lithium ion concentration changes in grain boundary-like features, where a bigger opening of the hysteresis loop was also observed, reflecting larger extents of lithium ion redistribution underneath the charged scanning probe. Interestingly, such loop opening was also observed to increase with cyclic number, accompanied by drop in capacity, suggesting that the nanoscale ESM measurement does correlate with macroscopic battery performance. Such strain-based detection offers much higher spatial resolution compared to conventional current-based electrochemical testing, which is very difficult to scale down to nanometer regime. Since then, they have also reported detailed studies on $LiCoO_2$ cathode [4], where local hot spots in electrochemical activities were observed. Using such technique, Zhu et al. [107,108] studied $LiNi_{1/3}Co_{1/3}Mn_{1/3}O_2$ thin film cathode and TiO_2 anode, as shown in Fig. 18, and observed that the quality factor decreases with the cyclic number, suggesting higher dissipation resulted from cycling.

Chen et al. have used DART ESM to study an inhomogeneous $LiFePO_4$ cathode consisting of micro- and nano-crystallized particles in the as-processed, charged, and discharged state [28], and uncovered drastic differences in ESM response and energy dissipation between micro- and nano-crystalline $LiFePO_4$. For example, in the as-processed sample, the averaged ESM response in the nano-crystalline area is more than twice the response in the microcrystalline area. After charging, the averaged amplitude drops substantially in both areas due to extraction of Li-ions. In the discharged state, substantially higher ESM response of more than 70% again is observed in the nano-crystalline area. Such correlation between nanoscale ESM response and local crystalline morphologies may help explain the superior capacity observed in Li-ion batteries with nano-crystalline $LiFePO_4$.

In addition to inducing lithium ion redistribution, the charged scanning probe may also trigger electrochemical reaction on the surface, which can be used as a nanolithography tool to pattern electrochemical system, similar to PFM nanolithography discussed earlier. One such example was demonstrated in lithium ion conducting glass ceramic (LICGC) [109], as shown in Fig. 19. It illustrates the topography of LICGC before and after measurement of the IV curves over a 100-point grid using a maximum voltage of 6 V, and shows that lithium particles were formed on 96 out of 100 points on the surface due to electrochemical reduction, with the four non-particle locations correlating with the presence of non-conductive $AlPO_4$ moieties. This demonstrates the feasibility of ESM as a nanolithography tool as well.

3.2.2. Solid oxide fuel cells

While originally envisioned for lithium ion batteries, it has since been realized that ESM can also be applied to study

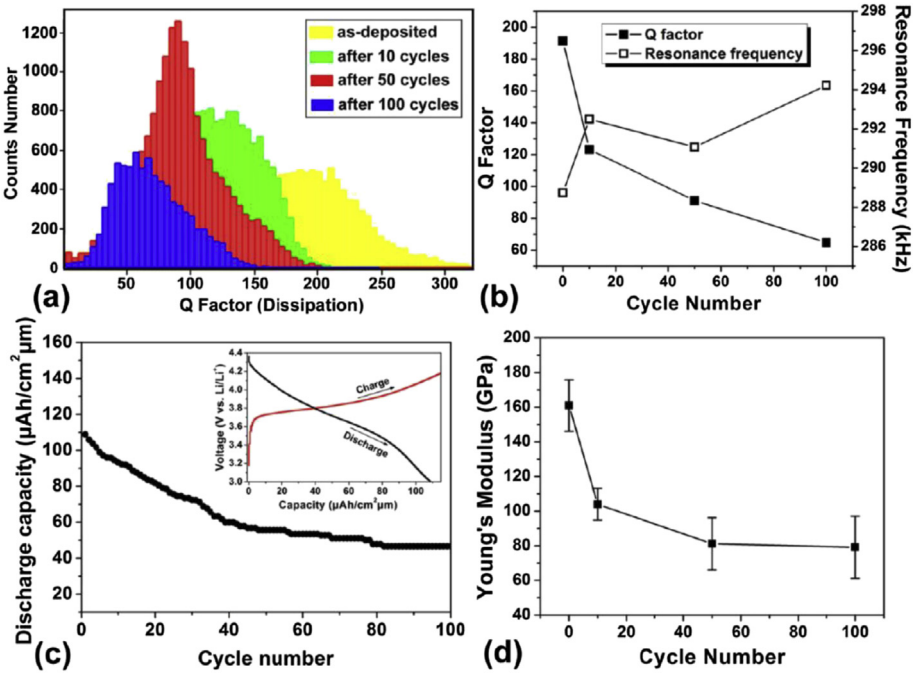

Fig. 18. (a) Histograms of quality factor distribution of the $LiNi_{1/3}Co_{1/3}Mn_{1/3}O_2$ thin film cathode at different cycling stages; (b) changes of resonance frequency and quality factor versus cycling number; (c) charge/discharge cycling performance of the $LiNi_{1/3}Co_{1/3}Mn_{1/3}O_2$ thin film cathode; the inset is the voltage-capacity profile during the first charge/discharge cycle; and (d) nanoindentation measured Young's modulus versus cycling number. Reprinted with permission from Ref. [107], ACS Nano 2013;7:1666–75. Copyright (2013) American Chemical Society.

other electrochemical systems as well, particularly solid oxide fuel cells. This was first demonstrated in oxygen conducting yttrium-stabilized zirconia (YSZ) [110], where systematic mapping of oxygen activity on bare and platinum-functionalized YSZ surfaces was demonstrated, allowing direct visualization of the oxygen reduction/evolution reaction activation process. The imaging mechanism was proposed to be based on generation or annihilation of oxygen vacancies depending on the sign of the bias, which diffuse and migrate through the material under the combined effect of the electric field and concentration gradient, though it is unclear whether the vacancies has sufficient mobility at lower temperatures. The associated changes in molar volume then result in electrochemical strain that is detected by ESM, and higher activity

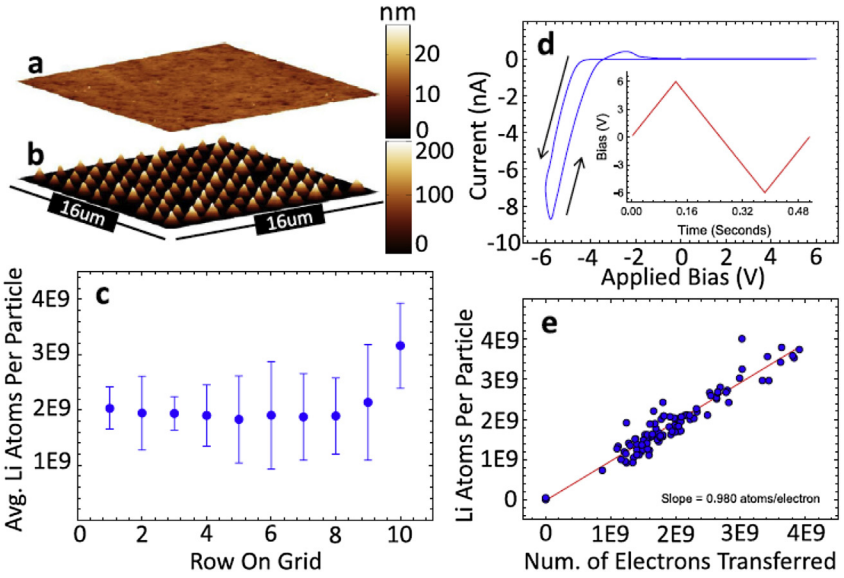

Fig. 19. (a) Topography of LICGC prior to the 100-point IV curve grid; (b) topography after IV measurements; (c) average particle size across the grid; (d) 100-point average IV response curve; (e) correlation of Li atoms per particle to the number of electrons transferred at each point on grid. Reprinted with permission from Ref. [109], Nanotechnology 2012;23:325402.

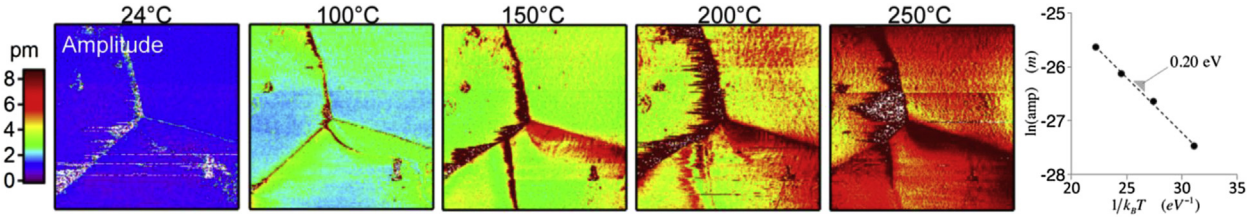

Fig. 20. ESM maps of ceria as a function of temperature. The Arrhenius plot at right shows the average strain amplitude (in pm) over the image area versus temperature. Reprinted with permission from Ref. [113], Appl. Phys. Lett. 2014;105:201602. Copyright [2014], AIP Publishing LLC.

at the triple-phase boundary was noted. The technique has also been applied to mixed electronic–ionic conductors such as $La_xSr_{1-x}CoO_3$ and oxygen conducting Ceria [111,112].

Nanocrystalline ceria exhibits conductivity orders of magnitude higher than microcrystalline ceria in air at high temperature, and the most widely accepted theory attributes this enhancement to relatively immobile positively charged defects and/or impurities accumulating at the grain boundary. This leads to a counterbalancing increase in the number of mobile electrons (small polarons) within a diffuse space charge region adjacent to each grain boundary, though such space charge regions have not been directly observed. Chen et al. applied ESM to image the location and relative population of mobile electrons near grain boundaries in polycrystalline Sm-doped ceria in air at 20–200 °C [113], and presented direct and spatially resolved evidence that such diffuse space charge regions do exist in ceria, and are localized to both grain boundaries and the gas-exposed surface, as shown in Fig. 20. A significant increase in signal intensity with temperature is observed, and the logarithm of the average signal intensity is fairly linear with 1/T, exhibiting an Arrhenius slope of approximately 0.2 eV. Such strain was attributed to potential-induced changes in small polaron concentration in the space-charge region near the gas-exposed surface and at grain boundaries, consistent with the activation energy estimated from Arrhenius slope. In general, applications of ESM to solid oxide fuel cells are limited by the temperature that can be applied to the samples, currently limited to below 300 °C. It will be really beneficial if this temperature range can be extended to 500 °C and higher.

4. Challenges and opportunities

As we have shown above, s-SPM techniques have been very successful in probing functional materials, biological structures, and electrochemical systems. However, a number of challenges remain. Here we focus on two critical issues - resolving microscopic mechanisms and quantitative analysis, which also offer great opportunities for future research.

4.1. Resolving microscopic mechanisms

As we have already noted, PFM and ESM operate in similar manners, and yield similar responses, making it difficult to distinguish two very different microscopic mechanisms. To appreciate this, we highlight recent experimental observations of electromechanical coupling and its apparent polarity switching in some unexpected materials, for example glass, silicon, electrets, and others [114–117]. None of these materials are piezoelectric or ferroelectric, yet they not only respond to local electrical excitation applied via SPM probe, but also have their strain response phase reversed by an electric field, resulting in apparent hysteresis and butterfly loops that resemble characteristics of classical ferroelectrics. It is thus important to distinguish the microscopic mechanisms of observed s-SPM responses, separating piezoelectric contributions from the electrochemical ones, which is rather difficult to do.

The situation is illustrated in Fig. 21, where typical mappings of vertical s-SPM amplitude and phase are shown for three representative classes of materials, including a classical ferroelectric PZT film, a lithium ion phosphate cathode material for lithium ion batteries, and an ionic glass [26]. No clear distinctions of electromechanical responses among these three systems are observed, except that the mappings of PZT show polycrystalline structure, while those of glass reveal no topographic features due to its amorphous nature. So can we determine the microscopic mechanisms of electromechanical coupling using s-SPM, especially when a material is new or unknown?

The response of s-SPM can come from both intrinsic material effects and extrinsic factors such as electrostatic interactions. We focus on the intrinsic material responses first, which can be classified into dielectric responses and electrochemical phenomena. Classical ferroelectrics exhibit piezoelectric strain biased by their spontaneous polarization, and thus exhibits bipolar characteristics that can be switched by an external DC voltage. Electrochemical systems, on the other hand, may possess Vegard strain that depends only on the ionic composition, and thus is nonpolar in nature. This will help distinguish between these two different mechanisms. The electrochemical process, however, can also induce ionic dipole moments, which can be switched by external DC voltage too. Electromechanical strains from both induced and spontaneous polarizations are electrostrictive, and thus are quadratic to the polarization,

$$\varepsilon \propto (P_s + \chi E)^2 = P_s^2 + 2\chi P_s E + \chi^2 E^2 \quad (8)$$

where P_s is spontaneous polarization and χE is the induced one. For classical ferroelectrics with large spontaneous polarization under small AC fields, the strain is predominantly

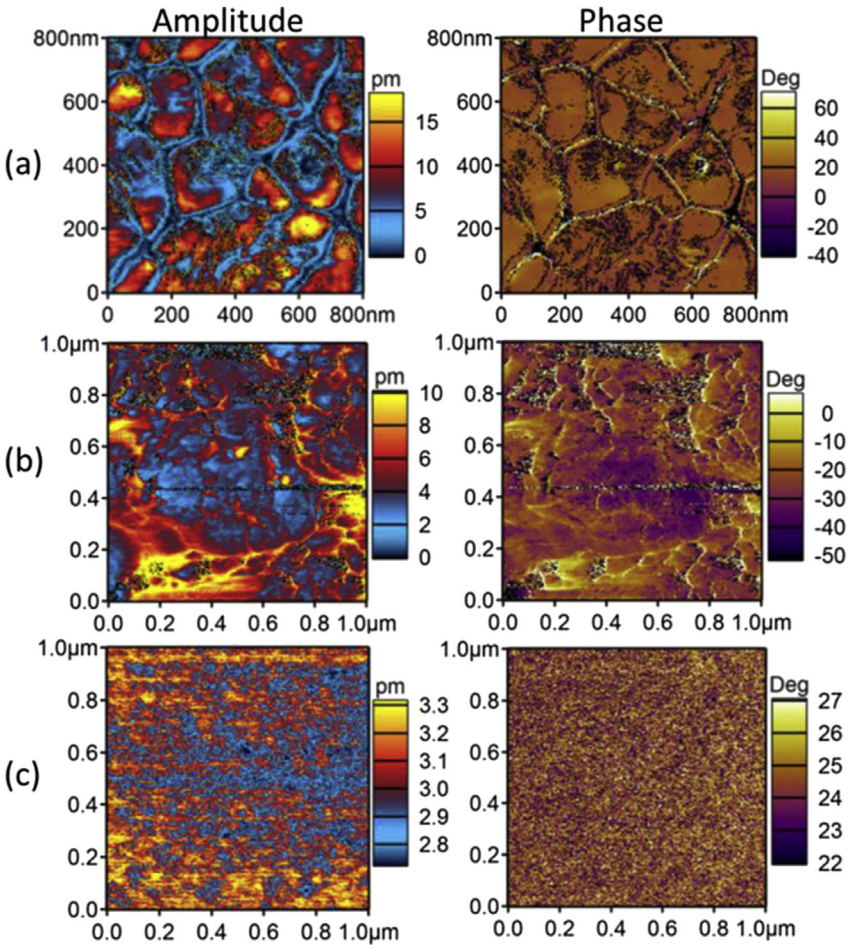

Fig. 21. Vertical s-SPM amplitude and phase mappings of electromechanical responses of three representative material systems; (a) PZT; (b) LiFePO4; and (c) soda-lime glass. Reprinted with permission from Appl. Phys. Lett. 2014:**104**:242907. Copyright 2014, AIP Publishing LLC.

linear to the AC field. On the other hand, for materials with small spontaneous polarization in comparison with the induced one, significant strain responses quadratic to the AC field would be expected. This will help distinguish contributions from spontaneous and induced polarization.

Based on these considerations, Chen et al. outlined a few methods to distinguish different microscopic mechanisms responsible for s-SPM response [26]. First of all, due to the nonpolar characteristic of electrochemical Vegard strain, DC field can only manipulate the ionic concentration and correspondingly the magnitude of its strain response, not its phase. As a result, a Vegard strain type of response should show no phase reversal under DC voltage, unlike a ferroelectric. Secondly, electrochemical dipoles can be induced by electric field, resulting in apparent phase reversal upon DC reversal. However, such strain is dominated by quadratic electrostrictive response, and thus have a large second harmonic component, while a typical piezoelectric has negligible second harmonic response, as shown in Fig. 22. Furthermore, induced dipoles in an amorphous system such as glass tend to have rather high macroscopic symmetry, with the symmetry axis aligned with the applied electric field. And thus the lateral shear response in-plane, if any, will be much smaller than the vertical one out of plane. This is in contrast to typical ferroelectrics such as PZT, for which substantial lateral responses comparable to the vertical ones are expected due to lower symmetry. Finally, electrochemical systems have rather different time dependence from that of piezoelectric materials, which makes it possible to further identify different microscopic mechanisms by varying the duration of the applied voltage. As such, by employing a combination of spectroscopic studies and their time dependences, examining first and second harmonic strain responses, and comparing vertical and lateral amplitudes, it is possible to distinguish electromechanical coupling arising from spontaneous polarization, induced dipole moment, and ionic Vegard strain, and these offer a clear guidance on using s-SPM techniques to study a wide range of functional materials and systems.

Extrinsic effects can also make large contributions to the s-SPM response. For example, it has recently been shown that the system-inherent background in PFM can originate from the interactions between the modulation voltage from the SPM probe and surface absorptions [118]. By minimizing such interactions via modulating voltage through bottom electrodes instead of scanning probe, background-free PFM results were obtained. Another important contribution is electrostatic

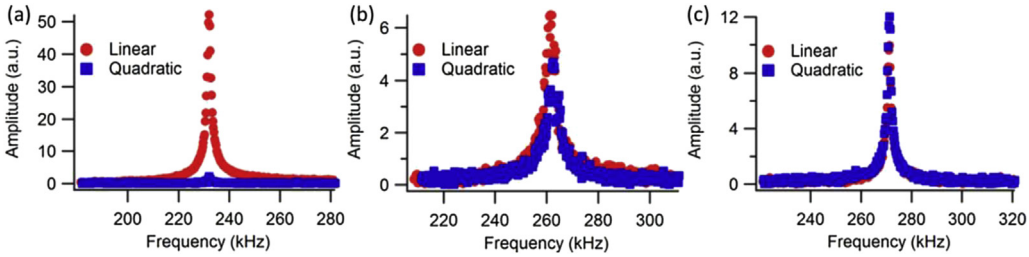

Fig. 22. First and second harmonic responses of three representative material systems in vertical s-SPM; (a) PZT; (b) LFP; and (c) soda-lime glass. Reprinted with permission from Appl. Phys. Lett. 2014:**104**:242907. Copyright 2014, AIP Publishing LLC.

interaction, which can be taken into account by contact mode Kelvin probe force microscopy [119].

Finally, we point out the importance of determining absolute phase for ESM [120], critical for identifying appropriate microscopic mechanisms responsible for electrochemical strain. Because of cantilever-sample resonance during dynamic measurement, such phase information is lost, and Chen et al. recently developed a procedure for calibrating such phase information at low frequency, where instrumental delay has been taken into account [115].

4.2. Quantitative analysis

While s-SPM has been widely applied to study a variety of materials and systems, the interpretation of s-SPM data, especially quantitative analysis, is not well established. The difficulty lies in four aspects: (1) the highly concentrated electric field underneath the conductive probe tip, (2) localized displacement field that is severely constrained by its surrounding, (3) complicated electromechanical coupling in the sample that could be nonlinear, and (4) coupling of the sample with the electric field in the air. As a result, although it is possible to estimate the effective piezoelectric coefficient from the field induced-displacement under PFM, such an effective coefficient does not only depend on the intrinsic piezoelectric constants of the samples, but also on a number of other electromechanical moduli as well as on the experimental conditions. In fact, analyses suggest that the relationship between the effective piezoelectric coefficients derived from PFM and the electromechanical moduli can be highly nonlinear, even when the constitutive behavior of the specimen is strictly linear [121,122]. For electrochemical systems involving ionic diffusion and migration, as well as possible contributions from surface reactions and space charges, the situation becomes even more complicated. This highlights the importance of rigorous theoretical analyses and computations of s-SPM under realistic experimental conditions and microscopic approximations, without which what one can learn from it would be rather limited and remain largely qualitative.

There have been a number of attempts to analyze electromechanical interactions between the charged SPM tip and probed specimens [123–125], and most of the analyses were built on decoupled methods with the charged SPM approximated as an effective point charge [121]. The electromechanical strain is treated as an Eigen-strain in an isotropic elastic solid, making the analysis considerably simpler. For example, a one-dimensional decoupled analysis has been carried out by Ganpule et al. [126] and Agronin et al. [127] to analyze the displacement of 90° domains under PFM and to determine the effective piezoelectric coefficient. The surface displacement of single crystal barium titanate has been analyzed by Felten et al. [128] using the decoupled method in 3D based on the elastically isotropic Green's function in half-space. Such decoupled methods have also been applied to study static domain imaging [129], domain dynamics [130,131], as well as PFM resolution [132,133]. Recent efforts have been focused on extending such analysis into ESM, wherein microscopic processes are completely different, involving diffusion and electromigration [134,135]. Nonlinear effects, such as electrostriction and electrostatic responses, have also been considered [136,137]. However, since direct electromechanical coupling is ignored, it is not clear how accurate such decoupled methods are.

Kalinin et al. [121] and Karapetian et al. [125] did carry out coupled electromechanical analysis of PFM under strong indentation conditions with given penetration depths, which enable them to ignore the coupling between the piezoelectric specimen and air. This analysis has recently been extended to local thermal and electrochemical probes that are relevant for ESM [138]. The weak indentation conditions that are more appropriate for s-SPM, and for which the sample-air coupling cannot be ignored, have been studied by Pan et al. [139], who analyzed electromechanical coupling of the transversely isotropic piezoelectric solid and the concentrated electric field induced by SPM tip, utilizing the fully coupled half-space Green's function in piezoelectric solids. The analysis can be extended to analyze ESM as well.

Even the fully coupled analysis of Pan et al. treated the conductive SPM probe as a point charge [139], which is a considerable simplification compared to reality. More accurate treatments would be desirable, especially when taking into account realistic configurations of the cantilever-sample system, as well as the dynamics associated with it. An analytic approach for such complicated systems is probably not realistic, and computational approaches utilizing finite element methods (FEM) and phase field techniques would be ideal. The dynamic response of an SPM cantilever interacting with a piezoelectric sample has recently been computed by FEM, yielding a spectrum of frequency dependent responses that have helped interpret both vertical and lateral PFM data [35]. In addition, the combination of phase field simulations with s-SPM has been very powerful in revealing formation and

evolution of domain structures in a ferroelectric thin film under a charged scanning probe, as demonstrated by Chen's group [140] and others [141,142], and we think this line of research will continue to produce fruitful results for understanding microscopic processes induced by the charged scanning probe, not only for PFM, but also ESM.

5. Concluding remarks

We close by reaffirming s-SPM as a powerful tool to probe functional materials, biological systems, and electrochemical devices with high sensitivity and spatial resolution, and by highlighting the challenges associated with quantitative analysis and resolving distinct microscopic mechanisms. Through combined experiments, analysis, and computation, we expect s-SPM to provide great insight into functional materials and structures in the years to come, and we believe it will play a valuable role in the emerging field of materiomics.

Acknowledgment

Part of the work was carried out under the support of NSF (CMMI-1100339 and CBET-1435968). JFL acknowledges the support of National Nature Science Foundation of China (Grants no. 51332002, 51221291). SHX acknowledges Natural Science Foundation of China (Approval Nos. 11472236, 11372268) and Provincial Natural Science Foundation of Hunan (13JJ1019).

References

[1] Guthner P, Dransfeld K. Local poling of ferroelectric polymers by scanning force microscopy. Appl Phys Lett 1992;61:1137–9.
[2] Kolosov O, Gruverman A, Hatano J, Takahashi K, Tokumoto H. Nanoscale visualization and control of ferroelectric domains by atomic-force microscopy. Phys Rev Lett 1995;74:4309–12.
[3] Balke N, Jesse S, Kim Y, Adamczyk L, Tselev A, Ivanov IN, et al. Real space mapping of Li-ion transport in amorphous Si anodes with nanometer resolution. Nano Lett 2010;10:3420–5.
[4] Balke N, Jesse S, Morozovska AN, Eliseev E, Chung DW, Kim Y, et al. Nanoscale mapping of ion diffusion in a lithium-ion battery cathode. Nat Nanotechnol 2010;5:749–54.
[5] Chen NQ, Ma FY, Xie SH, Liu YM, Proksch R, Li JY. High sensitivity piezomagnetic force microscopy for quantitative probing of magnetic materials at the nanoscale. Nanoscale 2013;5:5747–51.
[6] Eshghinejad A, Liang WI, Chen QN, Ma FY, Liu YM, Xie SH, et al. Piezoelectric and piezomagnetic force microscopies of multiferroic $BiFeO_3$–$LiMn_2O_4$ heterostructures. J Appl Phys 2014;116:066805.
[7] Damjanovic D. Ferroelectric, dielectric and piezoelectric properties of ferroelectric thin films and ceramics. Rep Prog Phys 1998;9:1267–324.
[8] Bishop SR, Duncan KL, Wachsman ED. Defect equilibria and chemical expansion in non-stoichiometric undoped and gadolinium-doped cerium oxide. Electrochim Acta 2009;54:1436–43.
[9] Zuev AY, Vylkov AI, Petrov AN, Tsvetkov DS. Defect structure and defect-induced expansion of undoped oxygen deficient perovskite $LaCoO_{3-\delta}$. Solid State Ionics 2008;179:1876–9.
[10] Lein HL, Wiik K, Grande T. Thermal and chemical expansion of mixed conducting $La_{0.5}Sr_{0.5}Fe_{1-x}Co_xO_{3-\delta}$ materials. Solid State Ionics 2006;177:1795–8.
[11] Cheng YT, Verbrugge MW. Evolution of stress within a spherical insertion electrode particle under potentiostatic and galvanostatic operation. J Power Sources 2009;190:453–60.
[12] Zhang XC, Sastry AM, Shyy W. Intercalation-induced stress and heat generation within single lithium-ion battery cathode particles. J Electrochem Soc 2008;155:A542–52.
[13] Plonsey R, Barr RC. Bioelectricity: a quantitative approach. New York: Kluwer; 2000.
[14] Sachs F, Brownell WE, Petrov AG. Membrane electromechanics in biology, with a focus on hearing. MRS Bull 2009;34:665–70.
[15] Liberman MC, Gao J, He DZZ, Wu XD, Jia SP, Zuo J. Prestin is required for electromotility of the outer hair cell and for the cochlear amplifier. Nature 2002;419:300–4.
[16] Haugstad G. Atomic force microscopy: understanding basic modes and advanced applications. New York: John Wiley & Sons; 2012.
[17] Yamanaka K, Nakano S. Quantitative elasticity evaluation by contact resonance in an atomic force microscope. Appl Phys A 1998;66:S313–7.
[18] Kos AB, Hurley DC. Nanomechanical mapping with resonance tracking scanned probe microscope. Meas Sci Technol 2008;19:015504.
[19] Hartmann U. Magnetic force microscopy. Annu Rev Mater Sci 1999;29:53–87.
[20] Gannepalli A, Yablon DG, Tsou AH, Proksch R. Mapping nanoscale elasticity and dissipation using dual frequency contact resonance AFM. Nanotechnology 2011;22:355705.
[21] Xie SH, Gannepalli A, Chen QN, Liu YM, Zhou YC, Proksch R, et al. High resolution quantitative piezoresponse force microscopy of $BiFeO_3$ nanofibers with dramatically enhanced sensitivity. Nanoscale 2012;4:408–13.
[22] Kareem AU, Solares SD. Characterization of surface stiffness and probe-sample dissipation using the band excitation method of atomic force microscopy: a numerical analysis. Nanotechnology 2012;23:015706.
[23] Rodriguez BJ, Callahan C, Kalinin SV, Proksch R. Dual-frequency resonance-tracking atomic force microscopy. Nanotechnology 2007;18:475504.
[24] Jesse S, Kalinin SV, Proksch R, Baddorf AP, Rodriguez BJ. The band excitation method in scanning probe microscopy for rapid mapping of energy dissipation on the nanoscale. Nanotechnology 2007;18:435503.
[25] Kim Y, Kumar A, Tselev A, Kravchenko II , Han H, Vrejoiu I, et al. Nonlinear phenomena in multiferroic nanocapacitors: joule heating and electromechanical effects. ACS Nano 2011;5:9104–12.
[26] Chen QN, Ou Y, Ma FY, Li JY. Mechanisms of electromechanical coupling in strain based scanning probe microscopy. Appl Phys Lett 2014;104:242907.
[27] Jesse S, Baddorf AP, Kalinin SV. Switching spectroscopy piezoresponse force microscopy of ferroelectric materials. Appl Phys Lett 2006;88:062908.
[28] Chen QN, Liu YY, Liu YM, Xie SH, Cao GZ, Li JY. Delineating local electromigration for nanoscale probing of lithium ion intercalation and extraction by electrochemical strain microscopy. Appl Phys Lett 2012;101:063901.
[29] Li DB, Bonnell DA. Controlled patterning of ferroelectric domains: fundamental concepts and applications. Annu Rev Mater Res 2008;38:351–68.
[30] Kalinin SV, Rodriguez BJ, Jesse S, Shin J, Baddorf AP, Gupta P, et al. Vector piezoresponse force microscopy. Microsc Microanal 2006;12:206–20.
[31] Yu HF, Zeng HR, Chu RQ, Li GR, Yin QR. Progress in nanoscale piezoresponse force microscopy on ferroelectrics. J Inorg Mater 2005;20:257–66.
[32] Kalinin SV, Rodriguez BJ, Jesse S, Karapetian E, Mirman B, Eliseev EA, et al. Nanoscale electromechanics of ferroelectric and biological systems: a new dimension in scanning probe microscopy. Annu Rev Mater Res 2007;37:189–238.
[33] Batagiannis A, Wübbenhorst M, Hulliger J. Piezo-and pyroelectric microscopy. Curr Opin Solid St M 2010;14:107–15.
[34] Shvartsman VV, Dkhil B, Kholkin AL. Mesoscale domains and nature of the relaxor state by piezoresponse force microscopy. Annu Rev Mater Res 2013;43:423–49.
[35] Zelisko M, Hanlumyuang Y, Yang SB, Liu YM, Lei CH, Li JY, et al. Anomalous piezoelectricity in two-dimensional graphene nitride nanosheets. Nat Commun 2014;5:4284.

[36] Horiuchi S, Yoshinori T. Organic ferroelectrics. Nat Mater 2008;7:357–66.

[37] Horiuchi S, Tokunaga Y, Giovannetti G, Picozzi S, Itoh H, Shimano R, et al. Above-room-temperature ferroelectricity in a single-component molecular crystal. Nature 2010;463:789–92.

[38] Li JY, Liu YM, Zhang YH, Cai HL, Xiong RG. Molecular ferroelectrics: where electronics meet biology. Phys Chem Chem Phys 2013;15:20786–96.

[39] Fu DW, Cai HL, Liu YM, Ye Q, Zhang W, Zhang Y, et al. Diisopropylammonium bromide is a high-temperature molecular ferroelectric crystal. Science 2013;339:425–8.

[40] Piecha A, Gagor A, Jakubas R, Szklarz P. Room-temperature ferroelectricity in diisopropylammonium bromide. CrystEngComm 2013;15:940–4.

[41] Yu Q, Li JF, Zhu FY, Li JY. Domain evolution of tetragonal $Pb(Zr_xTi_{1-x})O_3$ piezoelectric thin films on $SrTiO_3$ (100) surfaces: combined effects of misfit strain and Zr/Ti ratio. J Mater Chem C 2014;2:5836–41.

[42] Vasudevan RK, Okatan MB, Liu YY, Jesse S, Yang JC, Liang WI, et al. Unraveling the origins of electromechanical response in mixed-phase bismuth ferrite. Phys Rev B 2013;88:020402.

[43] Huang YC, Liu YY, Lin YT, Liu HJ, He Q, Li JY, et al. Giant enhancement of ferroelectric retention in $BiFeO_3$ mixed-phase boundary. Adv Mater 2014;26:6335–40.

[44] Cheng LQ, Wang K, Li JF, Liu YM, Li JY. Piezoelectricity of lead-free (K, Na)NbO_3 nanoscale single crystals. J Mater Chem C 2014;2:9091–8.

[45] Gruverman A, Kalinin SV. Piezoresponse force microscopy and recent advances in nanoscale studies of ferroelectrics. J Mater Sci 2006;41:107–16.

[46] Gruverman A, Wu D, Scott JF. Piezoresponse force microscopy studies of switching behavior of ferroelectric capacitors on a 100-ns time scale. Phys Rev Lett 2008;100:097601.

[47] Zhu XH, Liu ZG, Ming NB. Perovskite oxide nanowires: synthesis, property and structural characterization. J Nanosci Nanotechnol 2010;10:4109–23.

[48] Foschini CR, Ramirez MA, Simoes SR, Varela JA, Longo E, Simoes AZ. Piezoresponse force microscopy characterization of rare-earth doped $BiFeO_3$ thin films grown by the soft chemical method. Ceram Inter 2013;39:2185–95.

[49] Eerenstein W, Mathur ND, Scott JF. Multiferroic and magnetoelectric materials. Nature 2006;442:759–65.

[50] Nan CW, Bichurin MI, Dong SX, Viehland D, Srinivasan G. Multiferroic magnetoelectric composites: historical perspective, status, and future directions. J Appl Phys 2008;103:031101.

[51] Wang KF, Liu JM, Ren ZF. Multiferroicity: the coupling between magnetic and polarization orders. Adv Phys 2009;58:321–448.

[52] Ramesh R, Nicola AS. Multiferroics: progress and prospects in thin films. Nat Mater 2007;6:21–9.

[53] Catalan G, Scott JF. Physics and applications of bismuth ferrite. Adv Mater 2009;21:2463–85.

[54] Choi T, Lee S, Choi YJ, Kiryukhin V, Cheong SW. Switchable ferroelectric diode and photovoltaic effect in $BiFeO_3$. Science 2009;324:63–6.

[55] Zeches RJ, Rossell MD, Zhang JX, Hatt AJ, He Q, Yang CH, et al. A strain-driven morphotropic phase boundary in $BiFeO_3$. Science 2009;326:977–80.

[56] Zhao T, Scholl A, Zavaliche F, Lee K, Barry M, Doran A, et al. Electrical control of antiferromagnetic domains in multiferroic $BiFeO_3$ films at room temperature. Nat Mater 2006;5:823–9.

[57] Chu YH, Martin LW, Holcomb MB, Gajek M, Han SJ, He Q, et al. Electric-field control of local ferromagnetism using a magnetoelectric multiferroic. Nat Mater 2008;7:478–82.

[58] Seidel J, Martin LW, He Q, Zhan Q, Chu YH, Rother A, et al. Conduction at domain walls in oxide multiferroics. Nat Mater 2009;8:229–34.

[59] Yang CH, Seidel J, Kim SY, Rossen PB, Yu P, Gajek M, et al. Electric modulation of conduction in multiferroic Ca-doped $BiFeO_3$ films. Nat Mater 2009;8:485–93.

[60] Xie SH, Liu YM, Liu XY, Zhou QF, Shung KK, Zhou YC, et al. Local two-way magnetoelectric couplings in multiferroic composites via scanning probe microscopy. J Appl Phys 2010;108:054108.

[61] Xie SH, Ma FY, Liu YM, Li JY. Multiferroic $CoFe_2O_4$–$Pb(Zr_{0.52}Ti_{0.48})O_3$ core-shell nanofibers and their magnetoelectric coupling. Nanoscale 2011;3:3152–8.

[62] Xie SH, Liu YM, Ou Y, Chen QN, Tan XL, Li JY. Magnetoelectric coupling of multilayered $Pb(Zr_{0.52}Ti_{0.48})O_3$–$CoFe_2O_4$ film by piezoresponse force microscopy under magnetic field. J Appl Phys 2012;112:074110.

[63] Caruntu G, Yourdkhani A, Vopsaroiu M, Srinivasan G. Probing the local strain-mediated magnetoelectric coupling in multiferroic nanocomposites by magnetic field-assisted piezoresponse force microscopy. Nanoscale 2012;4:3218–27.

[64] Yan F, Chen GN, Lu L, Finkel P, Spanier JE. Local probing of magnetoelectric coupling and magnetoelastic control of switching in $BiFeO_3$–$CoFe_2O_4$ thin-film nanocomposite. Appl Phys Lett 2013;103:042906.

[65] Zhu QF, Xie Y, Zhang J, Liu YM, Zhan QF, Miao HC, et al. Multiferroic $CoFe_2O_4$–$BiFeO_3$ core–shell nanofibers and their nanoscale magnetoelectric coupling. J Mater Res 2014;29:657–64.

[66] Miao HC, Zhou XL, Dong SX, Luo HS, Li FX. Magnetic-field-induced ferroelectric polarization reversal in magnetoelectric composites revealed by piezoresponse force microscopy. Nanoscale 2014;6:8515–20.

[67] Mousoulis C, Maleki T, Ziaie B, Neu CP. Atomic force microscopy-coupled microcoils for cellular-scale nuclear magnetic resonance spectroscopy. Appl Phys Lett 2013;102:143702.

[68] a Nelson CT, Gao P, Jokisaari JR, Heikes C, Adamo C, Melville A, et al. Domain dynamics during ferroelectric switching. Science 2011;334:968–71;
b Chang H, Kalinin SV, Yang S, Yu P, Bhattacharya S, Wu PP, et al. Watching domains grow: In-situ studies of polarization switching by combined scanning probe and scanning transmission electron microscopy. J Appl Phys 2011;110:052014.

[69] Vasudevan RK, Liu YY, Li JY, Liang WI, Kumar A, Jesse S, et al. Nanoscale control of phase variants in strain-engineered $BiFeO_3$. Nano Lett 2011;11:3346–54.

[70] Rankin C, Chou CH, Conklin D, Bonnell DA. Polarization and local reactivity on organic ferroelectric surfaces: ferroelectric nanolithography using poly (vinylidene fluoride). ACS Nano 2007;1:234–8.

[71] Jo JY, Chen P, Sichel RJ, Baek SH, Smith RT, Balke N, et al. Structural consequences of ferroelectric nanolithography. Nano Lett 2011;11:3080–4.

[72] (a) Giocondi JL, Rohrer GS. Spatial separation of photochemical oxidation and reduction reactions on the surface of ferroelectric $BaTiO_3$. J Phys Chem B 2001;105:8275–7;
(b) Kalinin SV, Bonnell DA, Alvarez T, Lei X, Hu Z, Shao R, et al. Ferroelectric lithography of multicomponent nanostructures. Adv Mater 2004;16:795–9;
(c) Lei XJ, Li DB, Shao R, Bonnell DA. In situ deposition/positioning of magnetic nanoparticles with ferroelectric nanolithography. J Mater Res 2005;20:712–8.

[73] Liu XY, Hatano H, Takekawa S, Ohuchi F, Kitamura K. Patterning of silver nanoparticles on visible light-sensitive Mn-doped lithium niobate photogalvanic crystals. Appl Phys Lett 2011;99:053102.

[74] Burgos H, Jubera M, Villarroel J, Garcia-Cabanes A, Agullo-Lopez F, Carrascosa M. Role of particle anisotropy and deposition method on the patterning of nano-objects by the photovoltaic effect in $LiNbO_3$. Opt Mater 2013;35:1700–5.

[75] Damm S, Carville NC, Rodriguez BJ, Manzo M, Gallo K, Rice JH. Plasmon enhanced Raman from Ag nanopatterns made using periodically poled lithium niobate and periodically proton exchanged template methods. J Phys Chem C 2012;116:26543–50.

[76] Liu XY, Kitamura K, Yu QM, Xu JJ, Osada M, Takahiro N, et al. Tunable and highly reproducible surface-enhanced Raman scattering substrates made from large-scale nanoparticle arrays based on periodically poled $LiNbO_3$ templates. Sci Techn Adv Mater 2013;14:055011.

[77] Damm S, Carville NC, Manzo M, Gallo K, Lopez SG, Keyes TE, et al. Surface enhanced luminescence and Raman scattering from ferroelectrically defined Ag nanopatterned arrays. Appl Phys Lett 2013;103:083105.
[78] Lu H, Bark CW, Esque de los Ojos D, Alcala J, Eom CB, Catalan G, et al. Mechanical writing of ferroelectric polarization. Science 2012;336:59–61.
[79] Fukada E, Yasuda I. On the piezoelectric effect of bone. J Phys Soc Jpn 1957;12:1158–62.
[80] Lang SB. Piezoelectricity, pyroelectricity and ferroelectricity in biomaterials- speculation on their biological significance. IEEE Trans Dielectr Electr Insul 2000;7:466–73.
[81] Athenstaedt H. Pyroelectric and piezoelectric behavior of human dental hard tissues. Arch Oral Biol 1971;16:495–501.
[82] Fukada E, Ueda H. Piezoelectric effect in muscle. Jpn J Appl Phys 1970;9:844–5.
[83] Zilberst RM. Piezoelectric activity in invertebrate exoskeletons. Nature 1972;235:174–5.
[84] Morris RW, Kittlema LR. Piezoelectric property of otoliths. Science 1967;158:368–70.
[85] Shamos MH, Lavine LS. Piezoelectricity as a fundamental property of biological tissues. Nature 1967;213:267–9.
[86] Halperin C, Mutchnik S, Agronin A, Molotskii M, Urenski P, Salai M, et al. Piezoelectric effect in human bones studied in nanometer scale. Nano Lett 2004;4:1253–6.
[87] Gruverman A, Wu D, Rodriguez BJ, Kalinin SV, Habelitz S. High-resolution imaging of proteins in human teeth by scanning probe microscopy. Biochem Biophys Res Commun 2007;352:142–6.
[88] Kalinin SV, Rodriguez BJ, Jesse S, Thundat T, Gruverman A. Electromechanical imaging of biological systems with sub-10 nm resolution. Appl Phys Lett 2005;87:053901.
[89] Rodriguez BJ, Kalinin SV, Shin J, Jesse S, Grichko V, Thundat, et al. Electromechanical imaging of biomaterials by scanning probe microscopy. J Struct Biol 2006;153:151–9.
[90] Minary-Jolandan M, Yu MF. Uncovering nanoscale electromechanical heterogeneity in the subfibrillar structure of collagen fibrils responsible for the piezoelectricity of bone. ACS Nano 2009;3:1859–63.
[91] Minary-Jolandan M, Yu MF. Nanoscale characterization of isolated individual type I collagen fibrils: polarization and piezoelectricity. Nanotechnology 2009;20:085706.
[92] Harnagea C, Vallieres M, Pfeffer CP, Wu D, Olsen BR, Pignolet A, et al. Two-dimensional nanoscale structural and functional imaging in individual collagen type I fibrils. Biophys J 2010;98:3070–7.
[93] Kalinin SV, Rodriguez BJ, Jesse S, Seal K, Proksch R, Hohlbauch S, et al. Towards local electromechanical probing of cellular and biomolecular systems in a liquid environment. Nanotechnology 2007;18:424020.
[94] Denning D, Alilat S, Habelitz S, Fertala A, Rodriguez BJ. Visualizing molecular polar order in tissues via electromechanical coupling. J Struct Biol 2012;180:409–19.
[95] Denning D, Paukshto MV, Habelitz S, Rodriguez BJ. Piezoelectric properties of aligned collagen membranes. J Biomed Mater Res B 2014;102:284–92.
[96] Denning D, Kilpatrick JI, Hsu T, Habelitz S, Fertala A, Rodriguez BJ. Piezoelectricity in collagen type II fibrils measured by scanning probe microscopy. J Appl Phys 2014;116:066818.
[97] Bystrov VS, Seyedhosseini E, Kopyl S, Bdikin IK, Kholkin AL. Piezoelectricity and ferroelectricity in biomaterials: molecular modeling and piezoresponse force microscopy measurements. J Appl Phys 2014;116:066803.
[98] Li T, Zeng K. Piezoelectric properties and surface potential of green abalone shell studied by scanning probe microscopy techniques. Acta Mater 2011;59:3667–79.
[99] Li T, Zeng KY. Nano-hierarchical structure and electromechanical coupling properties of clamshell. J Struct Biol 2012;180:73–83.
[100] Li T, Chen L, Zeng KY. In situ studies of nanoscale electromechanical behavior of nacre under flexural stresses using band excitation PFM. Acta Biomater 2013;9:5903–12.
[101] Li T, Zeng K. Nanoscale piezoelectric and ferroelectric behaviors of seashell by piezoresponse force microscopy. J Appl Phys 2013;113:187202.
[102] Zhou XL, Miao HC, Li FX. Nanoscale structural and functional mapping of nacre by scanning probe microscopy techniques. Nanoscale 2013;5:11885–93.
[103] Heredia A, Meunier V, Bdikin IK, Gracio J, Balke N, Jesse S, et al. Nanoscale ferroelectricity in crystalline gamma-glycine. Adv Funct Mater 2012;22:2996–3003.
[104] Liu YM, Zhang YH, Chow M, Chen QN, Li JY. Biological ferroelectricity uncovered in aortic walls by piezoresponse force microscopy. Phys Rev Lett 2012;108:078103.
[105] Liu YM, Wang YJ, Chow M, Chen QN, Ma FY, Zhang YH, et al. Glucose suppresses biological ferroelectricity in aortic elastin. Phys Rev Lett 2013;110:168101.
[106] Liu YM, Cai HL, Zelisko M, Wang YJ, Sun JL, Yan F, et al. Ferroelectric switching of elastin. Proc Natl Acad Sci 2014;111:E2780–6.
[107] Zhu J, Lu L, Zeng KY. Nanoscale mapping of lithium-ion diffusion in a cathode within an all-solid-state lithium-ion battery by advanced scanning probe microscopy techniques. ACS Nano 2013;7:1666–75.
[108] Zhu J, Feng JK, Lu L, Zeng KY. In situ study of topography, phase and volume changes of titanium dioxide anode in all-solid-state thin film lithium-ion battery by biased scanning probe microscopy. J Power Sources 2012;197:224–30.
[109] Arruda TM, Kumar A, Kalinin SV, Jesse S. The partially reversible formation of Li-metal particles on a solid Li electrolyte: applications toward nanobatteries. Nanotechnology 2012;23:325402.
[110] Kumar A, Ciucci F, Morozovska AN, Kalinin SV, Jesse S. Measuring oxygen reduction/evolution reactions on the nanoscale. Nat Chem 2011;3:707–13.
[111] Kumar A, Leonard D, Jesse S, Ciucci F, Eliseev EA, Morozovska AN, et al. Spatially resolved mapping of oxygen reduction/evolution reaction on solid-oxide fuel cell cathodes with sub-10 nm resolution. ACS Nano 2013;7:3808–14.
[112] Doria S, Yang N, Kumar A, Jesse S, Tebano A, Aruta C, et al. Nanoscale mapping of oxygen vacancy kinetics in nanocrystalline samarium doped ceria thin films. Appl Phys Lett 2013;103:171605.
[113] Chen QN, Adler SB, Li JY. Imaging space charge regions in Sm-doped ceria using electrochemical strain microscopy. Appl Phys Lett 2014;105:201602.
[114] Proksch R. Electrochemical strain microscopy of silica glasses. J Appl Phys 2014;116:066804.
[115] Sekhon JS, Aggarwal L, Sheet G. Voltage induced local hysteretic phase switching in silicon. Appl Phys Lett 2014;104:162908.
[116] Miao HC, Sun Y, Zhou XL, Li YW, Li FX. Piezoelectricity and ferroelectricity of cellular polypropylene electrets films characterized by piezoresponse force microscopy. J Appl Phys 2014;116:066820.
[117] Miao HC, Tan C, Zhou XL, Wei XY, Li FX. More ferroelectrics discovered by switching spectroscopy piezoresponse force microscopy? EPL 2014;108:27010.
[118] Wang WB, Geng YN, Wu WD. Background-free piezoresponse force microscopy for quantitative measurements. Appl Phys Lett 2014;104:072905.
[119] Balke N, Maksymovych P, Jesse S, Kravchenko II , Li Q, Kalinin SV. Exploring local electrostatic effects with scanning probe microscopy: implications for piezoresponse force microscopy and triboelectricity. ACS Nano 2014;8:10229–36.
[120] Proksch R. In-situ piezoresponse force microscopy cantilever shape profiling. arXiv Preprint arXiv 2014;1409:0133.
[121] Kalinin SV, Karapetian E, Kachanov M. Nanoelectromechanics of piezoresponse force microscopy. Phys Rev B 2004;70:184101.
[122] Pan K, Liu YY, Liu YM, Li JY. Analyzing piezoresponse force microscopy for reconstruction of probed ferroelectric structures. J Appl Phys 2012;112:052016.
[123] Karapetian E, Kachanov M, Kalinin SV. Nanoelectromechanics of piezoelectric indentation and applications to scanning probe microscopies of ferroelectric materials. Phil Mag 2005;85:1017–51.

[124] Tian LL, Vasudevarao A, Morozovska AN, Eliseev EA, Kalinin SV, Gopalan V. Nanoscale polarization profile across a 180 degrees ferroelectric domain wall extracted by quantitative piezoelectric force microscopy. J Appl Phys 2008;104:074110.
[125] Morozovska AN, Eliseev EA, Bravina SL, Kalinin SV. Landau-Ginzburg-Devonshire theory for electromechanical hysteresis loop formation in piezoresponse force microscopy of thin films. J Appl Phys 2011;110:052011.
[126] Ganpule CS, Nagarajan V, Li H, Ogale AS, Steinhauer DE, Aggarwal S, et al. Role of 90 degrees domains in lead zirconate titanate thin films. Appl Phys Lett 2000;77:292.
[127] Agronin A, Molotskii M, Rosenwaks Y, Strassburg E, Boag A, Mutchnik S, et al. Nanoscale piezoelectric coefficient measurements in ionic conducting ferroelectrics. J Appl Phys 2005;97:084312.
[128] Felten F, Schneider GA, Saldana JM, Kalinin SV. Modeling and measurement of surface displacements in $BaTiO_3$ bulk material in piezoresponse force microscopy. J Appl Phys 2004;96:563–8.
[129] Gruverman A, Auciello O, Ramesh R, Tokumoto H. Scanning force microscopy of domain structure in ferroelectric thin films: imaging and control. Nanotechnology 1997;8:A38–43.
[130] Bdikin IK, Kholkin AL, Morozovska AN, Svechnikov SV, Kim SH, Kalinin SV. Domain dynamics in piezoresponse force spectroscopy: quantitative deconvolution and hysteresis loop fine structure. Appl Phys Lett 2008;92:182909.
[131] Wicks S, Seal K, Jesse S, Anbusathaiah V, Leach S, Garcia RE, et al. Collective dynamics in nanostructured polycrystalline ferroelectric thin films using local time-resolved measurements and switching spectroscopy. Acta Mater 2010;58:67–75.
[132] Morozovska AN, Eliseev EA, Bravina SL, Kalinin SV. Resolution-function theory in piezoresponse force microscopy: wall imaging, spectroscopy, and lateral resolution. Phys Rev B 2007;75:174109.
[133] Pan K, Liu YM, Liu YY, Li JY. Resolving ferroelectric nanostructures via piezoresponse force microscopy–a numerical investigation. J Appl Phys 2013;113:187223.
[134] Morozovska AN, Eliseev EA, Bravina SL, Ciucci F, Svechnikov GS, Chen LQ, et al. Frequency dependent dynamical electromechanical response of mixed ionic-electronic conductors. J Appl Phys 2012;111:014107.
[135] Morozovska AN, Eliseev EA, Kalinin SV. Electrochemical strain microscopy with blocking electrodes: the role of electromigration and diffusion. J Appl Phys 2012;111:014114.
[136] Eliseev EA, Morozovska AN, Ievlev AV, Balke N, Maksymovych P, Tselev A, et al. Electrostrictive and electrostatic responses in contact mode voltage modulated scanning probe microscopies. Appl Phys Lett 2014;104:232901.
[137] Morozovska AN, Eliseev EA, Varenyk OV, Kim Y, Strelcov E, Tselev A, et al. Nonlinear space charge dynamics in mixed ionic-electronic conductors: resistive switching and ferroelectric-like hysteresis of electromechanical response. J Appl Phys 2014;116:066808.
[138] Karapetian E, Kalinin SV. Indentation of a punch with chemical or heat distribution at its base into transversely isotropic half-space: application to local thermal and electrochemical probes. J Appl Phys 2013;113:187201.
[139] Pan K, Liu YY, Xie SH, Liu YM, Li JY. The electromechanics of piezoresponse force microscopy for a transversely isotropic piezoelectric medium. Acta Mater 2013;61:7020–33.
[140] Chen LQ. Phase-field models for microstructure evolution. Annu Rev Mater Res 2002;32:113–40.
[141] Li JY, Lei CH, Li LJ, Shu YC, Liu YY. Unconventional phase field simulations of transforming materials with evolving microstructures. Acta Mech Sin 2012;28:915–27.
[142] Liu YY, Vasudevan RK, Pan K, Xie SH, Liang WI, Kumar A, et al. Controlling magnetoelectric coupling by nanoscale phase transformation in strain engineered bismuth ferrite. Nanoscale 2012;4:3175–83.

Dr. Jiangyu Li is a Professor of Mechanical Engineering in the University of Washington, Seattle, USA. He obtained bachelor degree from Department of Materials Science and Engineering, Tsinghua University, in 1994, and Ph.D. degree from Department of Mechanical Engineering, University of Colorado-Boulder, in 1998. He completed postdoctoral studies at University of California-San Diego and California Institute of Technology before joining University of Nebraska-Lincoln as an Assistant Professor in 2001. He moved to University of Washington in 2006, where he held Bryan T. McMinn Endowed Professorship from 2007 to 2010. He has published numerous papers in leading journals, and has been recognized by ASME Sia-Nasser Early Career Medal, ICCES Young Investigator Award, and ASME Best Paper Award. He is an Associate Editor of Journal of Applied Physics, and serves on the Editorial Board of Journal of Materiomics.